LJMU Research Online

Schellenberger, G, Bogdán, Á, ZuHone, JA, Oppenheimer, BD, Truong, N, Khabibullin, I, Jennings, F, Pillepich, A, Burchett, J, Carr, C, Chakraborty, P, Crain, R, Forman, W, Jones, C, Kilbourne, CA, Kraft, RP, Markevitch, M, Nagai, D, Nelson, D, Ogorzalek, A, Randall, S, Sarkar, A, Schaye, J, Veilleux, S, Vogelsberger, M, Wang, QD and Zhuravleva, I

 Mapping the Imprints of Stellar and Active Galactic Nucleus Feedback in the Circumgalactic Medium with X-Ray Microcalorimeters

http://researchonline.ljmu.ac.uk/id/eprint/24265/

Article

For more information please contact researchonline@ljmu.ac.uk

Mapping the Imprints of Stellar and Active Galactic Nucleus Feedback in the Circumgalactic Medium with X-Ray Microcalorimeters

Gerrit Schellenberger[1], Ákos Bogdán[1], John A. ZuHone[1], Benjamin D. Oppenheimer[2], Nhut Truong[3,4,5], Ildar Khabibullin[6,7,8], Fred Jennings[9], Annalisa Pillepich[5], Joseph Burchett[10], Christopher Carr[11], Priyanka Chakraborty[1], Robert Crain[12], William Forman[1], Christine Jones[1], Caroline A. Kilbourne[3], Ralph P. Kraft[1], Maxim Markevitch[3], Daisuke Nagai[13], Dylan Nelson[14], Anna Ogorzalek[3,15], Scott Randall[1], Arnab Sarkar[16], Joop Schaye[17], Sylvain Veilleux[18], Mark Vogelsberger[16], Q. Daniel Wang[19], and Irina Zhuravleva[20]

[1] Center for Astrophysics | Harvard & Smithsonian, 60 Garden Street, Cambridge, MA 02138, USA; gerrit.schellenberger@cfa.harvard.edu
[2] University of Colorado, Boulder, 2000 Colorado Avenue, Boulder, CO 80305, USA
[3] NASA Goddard Space Flight Center, Code 662, Greenbelt, MD 20771, USA
[4] Center for Space Sciences and Technology, University of Maryland, Baltimore County, MD 21250, USA
[5] Max-Planck-Institut für Astronomie, Königstuhl 17, D-69117 Heidelberg, Germany
[6] Universitäts-Sternwarte, Fakultät für Physik, Ludwig-Maximilians-Universität München, Scheinerstr.1, 81679 München, Germany
[7] Max-Planck-Institut für Astrophysik, Karl-Schwarzschild-Straße 1, 85748 Garching, Germany
[8] Space Research Institute (IKI), Profsoyuznaya 84/32, Moscow 117997, Russia
[9] Institute for Astronomy, University of Edinburgh, Royal Observatory, Blackford Hill, Edinburgh EH9 3HJ, UK
[10] Department of Astronomy, New Mexico State University, Las Cruces, NM 88001, USA
[11] Department of Astronomy, Columbia University, 550 West 120th Street, New York, NY 10027, USA
[12] Astrophysics Research Institute, Liverpool John Moores University, 146 Brownlow Hill, Liverpool L3 5RF, UK
[13] Department of Physics, Yale University, New Haven, CT 06520, USA
[14] Universität Heidelberg, Zentrum für Astronomie, Institut für theoretische Astrophysik, Albert-Ueberle-Str. 2, 69120 Heidelberg, Germany
[15] Department of Astronomy, University of Maryland, College Park, MD 20742-2421, USA
[16] Department of Physics, Kavli Institute for Astrophysics and Space Research, Massachusetts Institute of Technology, Cambridge, MA 02139, USA
[17] Leiden Observatory, Leiden University, Niels Bohrweg 2, NL-2333 CA Leiden, The Netherlands
[18] Department of Astronomy and Joint Space-Science Institute, University of Maryland, College Park, MD 20742, USA
[19] Astronomy Department, University of Massachusetts, Amherst, MA 01003, USA
[20] Department of Astronomy and Astrophysics, University of Chicago, Chicago, IL 60637, USA

Abstract

The Astro2020 Decadal Survey has identified the mapping of the circumgalactic medium (CGM; the gaseous plasma around galaxies) as a key objective. We explore the prospects for characterizing the CGM in and around nearby galaxy halos with a future large-grasp X-ray microcalorimeter. We create realistic mock observations from hydrodynamical simulations (EAGLE, IllustrisTNG, and Simba) that demonstrate a wide range of potential measurements, which will address the open questions in galaxy formation and evolution. By including all background and foreground components in our mock observations, we show why it is impossible to perform these measurements with current instruments, such as X-ray CCDs, and why only microcalorimeters will allow us to distinguish the faint CGM emission from the bright Milky Way (MW) foreground emission lines. We find that individual halos of MW mass can, on average and depending on star formation rate, be traced out to large radii, around R_{500}, and for larger galaxies even out to R_{200}, using prominent emission lines, such as O VII, or O VIII. Furthermore, we show that emission-line ratios for individual halos can reveal the radial temperature structure. Substructure measurements show that it will be possible to relate azimuthal variations to the feedback mode of the galaxy. We demonstrate the ability to construct temperature, velocity, and abundance ratio maps from spectral fitting for individual galaxy halos, which reveal rotation features, active galactic nucleus outbursts, and enrichment.

Unified Astronomy Thesaurus concepts: Circumgalactic medium (1879); Stellar feedback (1602); Active galactic nuclei (16)

1. Introduction

Structure formation models predict that galaxies reside in massive dark matter halos and are embedded in large-scale gaseous halos, the circumgalactic medium (CGM). The CGM plays a crucial role in the evolution of galaxies as gas flows through the CGM and regulates galaxy growth over cosmic time. To establish a comprehensive picture of the formation and evolution of galaxies, it is essential to probe the interplay between the stellar body, the supermassive black hole (SMBH), and the large-scale CGM. However, our understanding of the CGM, especially its hot X-ray-emitting component that is critical to the mass budget of galaxies, is still limited. This lack of knowledge poses major gaps in our understanding of galaxy formation and evolution. The importance of the CGM is highlighted by the fact that it plays key roles on a wide range of spatial scales, from small-scale processes (e.g., galactic winds driven by supernovae or SNe) to the largest scales of galaxies (e.g., the accretion of gas from large-scale structure filaments).

Theoretical studies hint that the CGM has a complex and multiphase structure. In Milky Way (MW)–type and more massive galaxies, the dominant phases of the CGM have characteristic temperatures of millions of degrees and are predominantly observable at X-ray wavelengths (e.g., Crain

et al. 2010; van de Voort & Schaye 2013; Nelson et al. 2018a; Oppenheimer et al. 2019; Wijers & Schaye 2022). Indeed, in the well-established picture of structure formation, dark matter halos accrete baryonic matter, which is thermalized in an accretion shock (White & Rees 1978; White & Frenk 1991). The characteristic temperature is determined by the gravitational potential of the galaxies and reaches X-ray temperatures ($\gtrsim 10^6$ K) for MW-type galaxies. Since the cooling time of the hot gas is much longer than the dynamical time, the CGM is expected to be quasi-static and should be observable around galaxies in the present-day Universe.

Theoretical studies suggest that the CGM is multiphase and, for MW-mass and more massive galaxies, the bulk of the CGM resides in the hot (10^6 K $< T < 10^7$ K) phases (Nelson et al. 2018a). Absorption studies carried out with the Cosmic Origin Spectrograph on the Hubble Space Telescope have probed the cooler phases (10^4 K $< T < 10^6$ K) of the CGM (e.g., Tumlinson et al. 2011; Xavier Prochaska et al. 2011; Putman et al. 2012; Werk et al. 2014, 2016; Prochaska et al. 2017). Stacking analyses of galaxies using Sunyaev–Zeldovich (SZ) measurements have indicated the presence of hot phases in the CGM (Wu et al. 2020; Bregman et al. 2022; Moser et al. 2022; Das et al. 2023). However, X-ray observations are best suited to mapping and exploring the physical characteristics of the hot phases of the CGM.

Because the importance of studying the X-ray-emitting large-scale gaseous component of galaxies was recognized decades ago, all major X-ray observatories have attempted to explore this component. Studies of elliptical (or quiescent) galaxies achieved significant success in the early days of X-ray astronomy (Nulsen et al. 1984; O'Sullivan et al. 2001). Observations of massive ellipticals with the Einstein and ROSAT observatories revealed the presence of gaseous X-ray halos that extend beyond the optical extent of galaxies out to $\sim$100 kpc (Forman et al. 1985; Trinchieri & Fabbiano 1985; Trinchieri et al. 1986; Canizares et al. 1987; Mathews 1990; Mathews & Brighenti 2003). These observations not only revealed the ubiquity of the gaseous halos, but also allowed characterizations of the physical properties of the X-ray gas and measurements of its mass. Follow-up observations with XMM-Newton and Chandra played a major role in further probing the gaseous emission around a larger sample of nearby massive elliptical galaxies (Anderson & Bregman 2011; Bogdán et al. 2013a, 2015, 2017; Kim & Fabbiano 2013; Goulding et al. 2016; Li et al. 2018; Li 2020; Mathur et al. 2023; Nicastro et al. 2023). Thanks to the subarcsecond angular resolution of Chandra, it became possible to clearly resolve and separate point-like sources, such as low-mass X-ray binaries and active galactic nuclei (AGNs), from the truly diffuse gaseous emission (Revnivtsev et al. 2009; Bogdán & Gilfanov 2011). This allowed more detailed studies of the X-ray-emitting interstellar medium (ISM) and the larger-scale CGM. However, a major hindrance to studying elliptical galaxies is that the dominant fraction of galaxies explored by Chandra and XMM-Newton reside in rich environments, such as galaxy groups or galaxy clusters. The presence of these group and cluster atmospheres makes it virtually impossible to differentiate the CGM component of the galaxy from the large-scale group or cluster emission. Because the group or cluster atmosphere will dominate the overall emission beyond the optical radius, it becomes impossible to separate these components from each other and determine their relative contributions. Additionally, the gaseous component around quiescent galaxies is likely a mix of the infalling primordial gas onto the dark matter halos and the ejected gas from evolved stars, which was shock heated to the kinetic temperature of the galaxy. Due to quenching mechanisms, most quiescent galaxies reside in galaxy groups and clusters, which are not ideal targets for probing the primordial gas.

As opposed to their quiescent counterparts, star-forming galaxies provide the ideal framework to probe the gas originating from primordial infall. The main advantage of disk (or star-forming) galaxies is their environment. While quiescent galaxies form through mergers, which happen at a higher likelihood in rich environments, due to the higher galaxy density, a substantial fraction of star-forming galaxies preferentially reside in relatively isolated environments. The CGM around disk galaxies has been probed in a wide range of observations. Using ROSAT observations, the X-ray gas around disk galaxies remained undetected (Benson et al. 2000). However, this posed a challenge to galaxy formation models that predicted bright enough gaseous halos to be observed around nearby disk galaxies (White & Frenk 1991; Crain et al. 2010; Vogelsberger et al. 2020). Revising these models and involving efficient feedback from SNe and, later, AGN feedback drastically decreased the predicted X-ray luminosity of the X-ray CGM, implying that nondetection by ROSAT was consistent with theoretical models (e.g., Crain et al. 2010; Oppenheimer et al. 2020). More sensitive observations with Chandra and XMM-Newton led to the detection of the CGM around isolated massive disk galaxies (e.g., Wang et al. 2001; Li et al. 2006, 2007; Crain et al. 2010). Most notably, the CGMs of two massive galaxies, NGC 1961 and NGC 6753, were detected and characterized out to about 50–60 kpc radius, which corresponds to about $0.15r_{200}$, where r_{200} is the radius within which the density is 200 times the critical density of the Universe and we consider it to be the virial radius of the galaxies. These studies not only detected the gas, but also measured the basic properties of the CGM, such as temperature and abundance, and established simple thermodynamic profiles beyond the optical radii of the galaxies (Anderson & Bregman 2011; Bogdán et al. 2013a, 2017; Anderson et al. 2015). Following these detections, the CGM of other disk galaxies was also explored, albeit to a much lesser extent, due to the lower signal-to-noise ratios (S/Ns) of these galaxies (e.g., Anderson & Bregman 2011; Anderson et al. 2012; Dai et al. 2012; Bogdán et al. 2013b, 2015; Li et al. 2017). Despite these successes, however, it is important to realize that all these detections explored massive galaxies (a few $\times 10^{11}$ M$_\odot$ in stellar mass), while X-ray observations could not detect the CGM emission around MW-type galaxies, with the exception of our own Galaxy (Das et al. 2019a, 2019b, 2021; Bhattacharyya et al. 2023).

The main challenge in detecting the extended CGM of external galaxies is due to the hot gas residing in our own MW. Specifically, our solar system is surrounded by the local hot bubble (LHB), which has a characteristic temperature of $kT \approx 0.1$ keV (McCammon et al. 2002; Das et al. 2019a). On larger scales, the MW also hosts an extended hot component with a characteristic temperature of $\sim$0.2 keV (McCammon et al. 2002; Das et al. 2019a). These gas temperatures are comparable to those expected from other external galaxies and, since both the MW and the other galaxies exhibit the same thermal emission component, the emission signal from the low-surface-brightness CGM of external galaxies can be orders of magnitude below the MW foreground emission. Because the

X-ray emission from the MW foreground is present in every sightline and this component cannot be differentiated at CCD resolution (∼50–100 eV), its contribution cannot be easily removed from the CGM component of other galaxies. A direct consequence of this is that even future telescopes with larger collecting areas with CCD-like instruments will be limited by the foreground emission and thus cannot probe the large-scale CGM. To achieve a transformative result in exploring the extended CGM, we must utilize high-spectral-resolution spectroscopy to spectroscopically differentiate the emission lines of the MW foreground from those emitted by the external galaxies. We emphasize that mapping the CGM around individual galaxies is essential for learning about its 2D distribution, enrichment, and thermodynamic structure, which is more challenging with dispersive (grating) spectroscopy due to line broadening (Li 2020) and is pursued by concepts such as ARCUS (Smith et al. 2022).

Recent advances in technology allow us to take this transformative step. The development of high-spectral-resolution X-ray integral field units (IFUs) provides the much-needed edge over traditional CCD-like instruments. Notably, X-ray IFUs can simultaneously provide traditional images with good spatial resolution and very high, 1–2 eV, spectral resolution across the array. In this work, we explore how utilizing the new technology of X-ray IFUs can drastically change our understanding of galaxy formation. We assume capabilities similar to the Line Emission Mapper (LEM) Probe mission concept (Kraft et al. 2022). The LEM concept is designed to have a large-field-of-view (FoV; ≳900 arcmin^2), state-of-the-art X-ray microcalorimeter, with 1 eV spectral resolution in the central array and 2 eV spectral resolution across the FoV. The single-instrument telescope is planned to have a 2500 cm^2 collecting area at 1 keV energy. Overall, the spectral resolution of LEM surpasses that of CCD-like instruments by 50–100 times, allowing us to spectrally separate the MW foreground lines and the emission lines from the CGM of external galaxies.

Modern cosmological hydrodynamical simulations are able to model the detailed distribution of the hot CGM (e.g., Cen & Ostriker 1999, 2000). The divergence among these simulations is chiefly driven by the difference in modeling baryonic physics, most notably the modeling of feedback processes, such as those driven by star formation activities or accretion onto SMBHs (see, e.g., Vogelsberger et al. 2020 for a recent review). The intrinsic limitations due to the finite resolution of these simulations require subresolution models, which add uncertainties to the results. Subresolution feedback effects are implemented to mimic net effects of AGN feedback, but depend on the numerical implementation. The simulations of the IllustrisTNG project, for example, switch from thermal to kinetic feedback mode, depending on the chosen threshold of the AGN accretion rate (Weinberger et al. 2017; Vogelsberger et al. 2020). Other simulations, such as EAGLE, use only the thermal AGN feedback channel to reheat the gas (Schaye et al. 2015). Thus, simulations are significantly diverse in predicting the CGM properties (e.g., X-ray line emission profiles; see van de Voort & Schaye 2013; Wijers & Schaye 2022; Truong et al. 2023). Therefore, probing the hot phases of the CGM is essential to understand how feedback processes operate on galactic scales, and future observations will constrain models by comparison of observations with simulations.

In this work, we utilize three modern hydrodynamical structure formation simulations—IllustrisTNG, EAGLE, and

Table 1
FoM for CGM Detection of Selected Past, Current, and Future X-Ray Missions and Concepts, Adapted from Li (2020)

Mission	$R = E/\Delta E$ (at 1 keV)	$A_{\rm eff}$ (cm^2)	$\Omega_{\rm FoV}$ (deg^2)	FoM (cm^2 deg^2)
Currently Operating Missions				
XMM-Newton	20	2000	0.20	8000
eROSITA	20	2000	0.79	31,000
XRISM	200	250	2×10^{-3}	125
Previously Proposed Missions				
Super DIOS	300	1000	0.25	75, 000
EDGE	330	1000	0.5	165,000
Currently Proposed Missions				
Athena/X-IFU	250	5800	4×10^{-3}	6400
HUBS	300	500	1	150,000
LEM	500	2500	0.25	312,000

Simba—to demonstrate that a large-grasp imaging microcalorimeter will provide an unprecedented view into the formation and evolution of galaxies. In Section 2, we describe the hydrodynamical simulations and the setup of the mock observations. We show the surface brightness profiles of four bright emission lines for galaxy subsamples selected by halo mass and star formation rate (SFR) in Section 3. We also quantify the level of substructure and present 2D maps of the temperature and element abundance ratios inferred from a spectral analysis. Section 4 discusses the results.

2. Methods

Here we describe our methodology for the analysis of microcalorimeter mock observations.

2.1. X-Ray Microcalorimeter

There are currently several X-ray missions and mission concepts with a microcalorimeter, such as Athena X-IFU (Barret et al. 2013, 2018, 2023), the X-Ray Imaging and Spectroscopy Mission (XRISM; Terada et al. 2021), the Hot Universe Baryon Surveyor (HUBS; Zhang et al. 2022), the Explorer of Diffuse Emission and Gamma Ray Burst Explosions (EDGE; Piro et al. 2007), Super DIOS (Sato et al. 2022), and the LEM (Kraft et al. 2022). However, the CGM can be best probed by a large-area, large-FoV instrument (i.e., large-grasp, which is the product of the FoV and collecting area), designed for the X-ray detection of the faint emission lines of the CGM. We follow the definition of Li (2020) for the figure of merit (FoM) to map the hot phase of the CGM, FoM = $R\, A_{\rm eff}\, \Omega_{\rm FoV}$, where the spectral resolving power $R = E/\Delta E$ is measured at 1 keV, the effective area $A_{\rm eff}$ at 1 keV is measured in cm^2, and the solid angle $\Omega_{\rm FoV}$ is measured in deg^2. Using this metric, it can be seen in Table 1 that a LEM-like mission is ideally suited to detecting and measuring the properties of the CGM. We use the LEM mission design to illustrate the power of a large-grasp microcalorimeter to probe the CGM. We note that the spectral resolution must allow the distinguishing of bright MW foreground lines from the typically fainter and redshifted CGM emission lines, namely C VI, O VII, O VIII, and Fe XVII. Therefore, a lower spectral resolution can in principle be compensated for by selecting more distant galaxies, which will be fainter and require deeper exposures. For comparison, we also include two current CCD

instruments in Table 1, XMM-Newton (Jansen et al. 2001; Lumb et al. 2012) and eROSITA (Predehl et al. 2021).

Spatial resolution is not a key parameter, as the point-source contribution (e.g., from AGNs) to X-ray flux from nearby galaxies can be modeled in narrow bands. However, a smaller point-spread function (PSF) is beneficial, as it allows spatial masking of the brightest point sources in the field from structure in the CGM. We note that in the case of LEM, the spatial resolution (half-power diameter) of $10''$ is also superior to most other missions listed in Table 1.

Although the LEM concept includes a high-resolution ($\sim 1\,\mathrm{eV}$) central array ($5' \times 5'$), we only consider the energy resolution of the main array (2 eV). A galaxy with similar stellar mass as the MW extends out to $R_{500} = 165\,\mathrm{kpc}$. At redshift $z = 0.01$, this galaxy will span $26'$ and fit well within the $32' \times 32'$ FoV. Therefore, we conservatively only consider a 2 eV resolution throughout the FoV. Larger and brighter galaxies at a redshift $z = 0.035$, which contain about twice the MW's stellar mass, can be tested for CGM emission even beyond R_{500}. Therefore, we investigate the CGM emission for galaxies at these two redshifts assuming a LEM-like instrument.

2.2. Mock Observations of Hydrodynamical Cosmological Simulations

2.2.1. Simulations

Our galaxy selection from the cosmological simulations follows clear criteria. We focus here on three state-of-the-art simulations: TNG100 of the IllustrisTNG project (Vogelsberger et al. 2014a, 2014b; Pillepich et al. 2017b, 2017a, 2018, 2019; Weinberger et al. 2017; Nelson et al. 2018b, 2019a, 2019b; Marinacci et al. 2018; Naiman et al. 2018; Springel et al. 2018; with $\sim 110.7\,\mathrm{cMpc}$ box size (comoving coordinates) and a baryon mass $m_{\mathrm{baryon}} = 1.4 \times 10^6\,M_\odot$), EAGLE-Ref-L100N1504 (EAGLE; Crain et al. 2015; Schaller et al. 2015; Schaye et al. 2015; McAlpine et al. 2016; Wijers & Schaye 2022; with $\sim 100\,\mathrm{Mpc}$ box size and a baryon mass $m_{\mathrm{baryon}} = 1.81 \times 10^6\,M_\odot$), and Simba 100 Mpc (Simba; Hopkins 2015; Davé et al. 2019; with $\sim 147\,\mathrm{Mpc}$ box size and a baryon mass $m_{\mathrm{baryon}} = 1.82 \times 10^7\,M_\odot$), which all have similar volumes and cosmological parameters, are tuned to reproduce observed stellar properties, but vary in hydrodynamic codes and modules for galaxy formation, including AGN feedback prescriptions (e.g., Davies et al. 2019a, 2019b; Zinger et al. 2020; Donnari et al. 2021; Truong et al. 2021; Byrohl & Nelson 2023). All three simulations trace the evolution of gas, stellar, dark matter, and SMBH particles over a large redshift range. Gas heating and cooling processes are included, as well as star formation and stellar evolution, and various feedback processes (AGN, SNe, and stellar winds). The implementation of the AGN feedback is significantly different in the three simulations, emphasizing the need for a detailed comparison of observables that can trace the feedback mechanisms. For example, EAGLE uses a thermal AGN feedback model with a single efficiency of mass to energy (Booth & Schaye 2009), while TNG and Simba have multiple energy injection modes (Oppenheimer et al. 2020; Truong et al. 2023). In order to understand the impact of stellar-driven and AGN feedback on the CGM, and how it can be traced with a large-grasp microcalorimeter, we subdivide the simulated galaxies into halo mass bins based on M_{200} (the total mass within 200 times the critical density of the Universe at the redshift of the galaxy).

2.2.2. Samples

In simulations (Donnari et al. 2021; Mitchell & Schaye 2022; Sorini et al. 2022; Ayromlou et al. 2023) and observations (Mandelbaum et al. 2006; Gavazzi et al. 2007; Zheng et al. 2007; Hansen et al. 2009; Guo et al. 2010; Wang & Jing 2010), a peak of the stellar mass fraction of nonsatellite galaxies is observed around the MW and M31 halo mass and stellar mass fraction (see Schödel et al. 2002; Licquia & Newman 2015; Posti & Helmi 2019 for MW properties; and Tamm et al. 2012; Rahmani et al. 2016; Al-Baidhany et al. 2020; Carlesi et al. 2022 for M31; both are indicated in Figures 1 and 2). MW and M31 analogs have been found by Ramesh et al. (2022) in TNG50 simulations with realistic multiphase gas properties, e.g., warm and cold gas reservoirs. The peak of the stellar mass fraction, and growing mass of the SMBHs, implies a transition from an SN-dominated mode of feedback to AGN-dominated feedback. This transition is poorly understood and only a detailed analysis of the CGM will reveal the driving mechanism of this feedback mode change. Therefore, we select three galaxy samples, based on halo mass, to encapsulate the different forms of the dominant feedback (see the blue, orange, and green regions in Figure 1).

We select galaxies with M_{200} from $10^{11.5}$ to $\times 10^{12}\,M_\odot$ as our low-mass sample (Figure 2 and Table 2). In this mass range, the stellar mass fraction increases with halo mass, which means more and more gas is converted into stars, indicating strong stellar feedback (see, e.g., Behroozi et al. 2010, 2019; Moster et al. 2010; Harrison 2017 and references therein). The galaxies in the low-mass sample also generally have lower central black hole masses (around $7 \times 10^7\,M_\odot$ in TNG100) and a high specific star formation rate (sSFR $\sim 6 \times 10^{-11}\,\mathrm{yr}^{-1}$, for instance, in the case of EAGLE), which are not representative of the typical galaxy across the three samples.

Galaxies in the mass range from $M_{200} = 10^{12}$ to $10^{12.5}\,M_\odot$ form our medium-mass sample (Figure 2 and Table 2) and generally are not clearly dominated by either one feedback mechanism. The impact of both stellar and AGN feedback on the CGM should be visible in these galaxies, which have significantly more massive central AGNs (a median at least three times as massive as in the low-mass sample; Table 2) and, depending on the simulation, also lower sSFRs.

Our high-mass sample consists of halo masses from $M_{200} = 10^{12.5}$ to $10^{13}\,M_\odot$ (Figure 2 and Table 2) and is generally dominated by AGN feedback, while star formation and stellar feedback become less and less important. The central black hole masses are on average a factor of 2.3 larger than in the medium-mass sample, while the sSFR decreases by a factor of 2 (see Figure 2).

From each simulation—TNG100, EAGLE, and Simba—we select 40 galaxies for each of the three samples. We also exclude any galaxy that is a noncentral galaxy of the dark matter halo, e.g., a member galaxy of a cluster that evolves very differently due to an early onset of quenching by the surrounding ICM. We note that the stated halo masses refer to the parent dark matter halo of each galaxy. By restricting our sample to halo masses below $10^{13}\,M_\odot$, we exclude all galaxies within clusters or groups. The galaxies have been selected to be uniformly distributed in $\log M_{200}$. Our samples are summarized in Table 2, and we describe all the individual galaxies in more detail in Tables 4, 5, and 6 in Appendix C and show the galaxy properties, including halo and stellar mass, SFR, and black hole mass, in Figure 2.
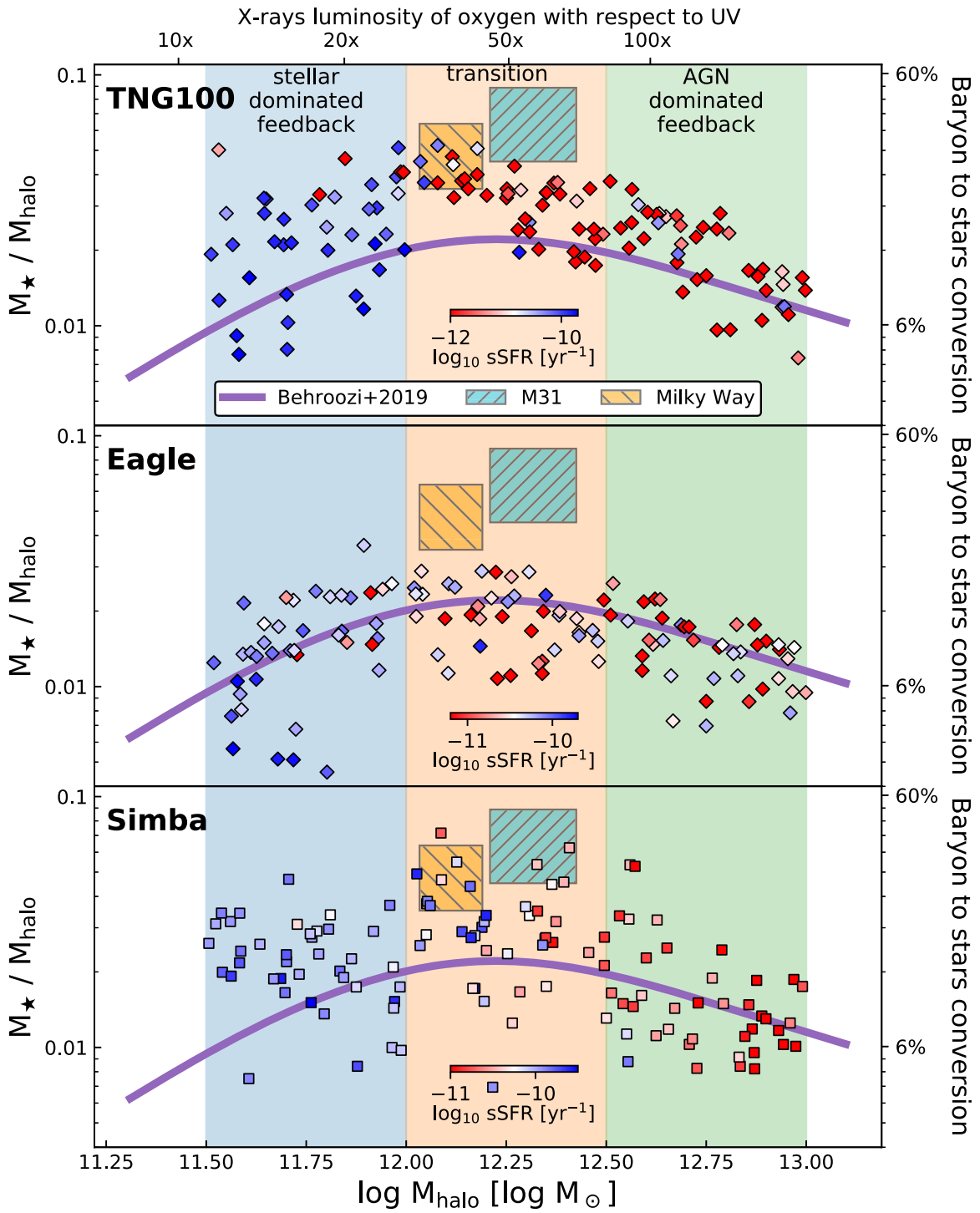
Figure 1. Stellar mass fraction as a function of the halo mass of the galaxies. The three panels (top, middle, and bottom) show the selected galaxies from TNG100, Eagle, and Simba, respectively. The blue-, orange-, and green-shaded halo mass bins represent the three feedback regimes that we explore. The baryon-to-star conversion efficiency on the right y-axis assumes a cosmic baryon fraction of $f_b = 0.17$. The top axis indicates the fraction the X-ray-emitting oxygen ions (O VII, O VIII) with respect to O VI, which is dominant in the UV (as predicted by Nelson et al. 2018a). The purple line shows the predictions from Behroozi et al. (2019) for $z = 0$ and excludes satellite galaxies within larger halos.

2.2.3. Mock X-Ray Observations

We produce mock observations from the hydro simulations using pyXSIM[21] (see ZuHone & Hallman 2016), which creates large photon samples from the 3D simulations. We create mock observations from a high-spectral-resolution imaging instrument assuming a Gaussian PSF with 10″ FWHM using SOXS.[22] We use a detector size of 128×128 pixels with 15″ per pixel, yielding an FoV of $32' \times 32'$. The spectral bandpass covered is 0.2–2 keV, with 2 eV FWHM resolution. The X-ray
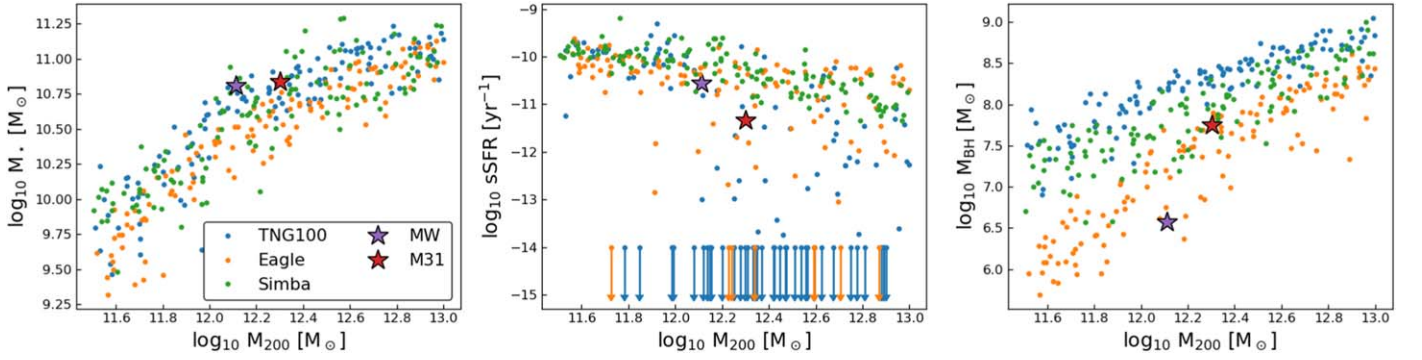
Figure 2. Properties of the galaxies in the three samples (low-, medium-, and high-mass) for each of the three simulations (TNG100 in blue, EAGLE in orange, and Simba in green). The x-axis of each of the three panels is the halo mass M_{200} in $\log_{10}$. The left panel shows the stellar mass dependence $M_\star$, similar to what is shown in 1. We also highlight the location of the MW (purple star) and M31 (red star). The middle panel illustrates the sSFR, in units per year, clearly decreasing with increasing halo mass. The right panel shows the SMBH mass dependence, clearly indicating different trends between the simulations, where EAGLE produces lower-mass black holes than TNG100.

Table 2
Galaxy Halo Samples for Tracing and Mapping the CGM Emission

Simulation Box		IllustrisTNG			EAGLE			Simba		
		TNG100			Ref-L0100N1504			100 Mpc h^{-1}		
		Low	Medium	High	Low	Medium	High	Low	Medium	High
Sample size		40	40	40	40	40	40	40	40	40
$\log_{10} M_{200}$	Median	11.79	12.29	12.73	11.72	12.26	12.76	11.76	12.21	12.73
$[\log_{10} M_\odot]$	25%	11.65	12.17	12.63	11.63	12.15	12.64	11.63	12.15	12.58
	75%	11.92	12.39	12.89	11.84	12.35	12.88	11.87	12.35	12.87
$\log_{10} M_\star$	Median	10.15	10.77	11.06	9.91	10.52	10.93	10.07	10.72	10.95
$[\log_{10} M_\odot]$	25%	9.94	10.71	10.95	9.64	10.41	10.80	9.96	10.60	10.74
	75%	10.32	10.85	11.11	10.09	10.65	10.97	10.21	10.84	11.05
$\log_{10}$ SFR	Median	−0.01	−3.95	−1.36	−0.32	0.03	0.15	0.22	0.61	0.33
$[M_\odot \, \mathrm{yr}^{-1}]$	25%	−0.34	-5.00	−5.00	-0.51	−0.61	-0.93	0.11	0.34	0.18
	75%	0.13	−0.71	-0.41	−0.12	0.32	0.50	0.33	0.78	0.66
$\log_{10} M_{BH}$	Median	7.73	8.33	8.68	6.33	7.46	8.14	7.38	7.94	8.43
$[\log_{10} M_\odot]$	25%	7.50	8.21	8.53	6.09	7.17	7.96	7.18	7.62	8.25
	75%	7.99	8.43	8.75	6.67	7.69	8.31	7.57	8.07	8.62
R_{500}	Median	123	176	242	116	170	250	117	166	238
[kpc]	25%	110	163	222	105	158	225	107	154	218
	75%	135	193	274	125	184	272	126	183	264
[arcmin]	Median	9.96	14.32	5.78	9.42	13.84	5.97	9.54	13.47	5.68

Note. For each quantity—the halo mass M_{200}, the stellar mass within 30 kpc $M_\star$, the halo SFR, the SMBH mass M_{BH}, and the characteristic radius R_{500}—we show the median value of the sample, as well as the 25th and 75th percentiles. To calculate R_{500} in arcmin, we place the high-mass samples at $z = 0.035$, while the low- and medium-mass samples are at $z = 0.01$.

emission is modeled from each emitting, non-star-forming gas cell with $T > 3 \times 10^5$ K and $\rho < 5 \times 10^{-25}$ g cm^{-3} (a value of the density close to the star formation density threshold in the TNG simulations). The electron and hydrogen number densities in each gas cell are determined from the underlying simulations (TNG100, EAGLE, and Simba; see Section 2.2.1), which track the conversion of gas into stars, starting from primordial initial abundance. The electron number density depends on the density, temperature, and abundance of the gas. The emission measure of each gas cell is calculated based on electron and hydrogen number densities. In each galaxy, there is also a small set of isolated gas cells that are abnormally bright in X-rays—these typically have extreme values of cooling time and/or thermal pressure, and on this basis are excluded from the analysis to improve visualizations, but we do

not find that leaving them in changes any of our conclusions (see ZuHone et al. 2023a for more details).

The plasma emission of the hot gas surrounding the galaxy is based on the Cloudy emission code (Ferland et al. 2017) and includes the effect of resonant scattering from the cosmic X-ray background (CXB), which enhances the O VIIr line (Chakraborty et al. 2020a, 2022). An extensive description is provided in Churazov et al. (2001) and Khabibullin & Churazov (2019). In contrast to other emission models, such as APEC/AtomDB (Foster et al. 2012, 2018), we utilize a density-dependent model, which is sensitive to the photoionization state of the gas at densities $\lesssim 10^{-4}$ cm^{-3} (see, e.g., Bogdan et al. 2023). We updated the code with respect to Khabibullin & Churazov (2019) to include the latest version of Cloudy and ensured that the intrinsic resolution matches the subelectronvolt requirements
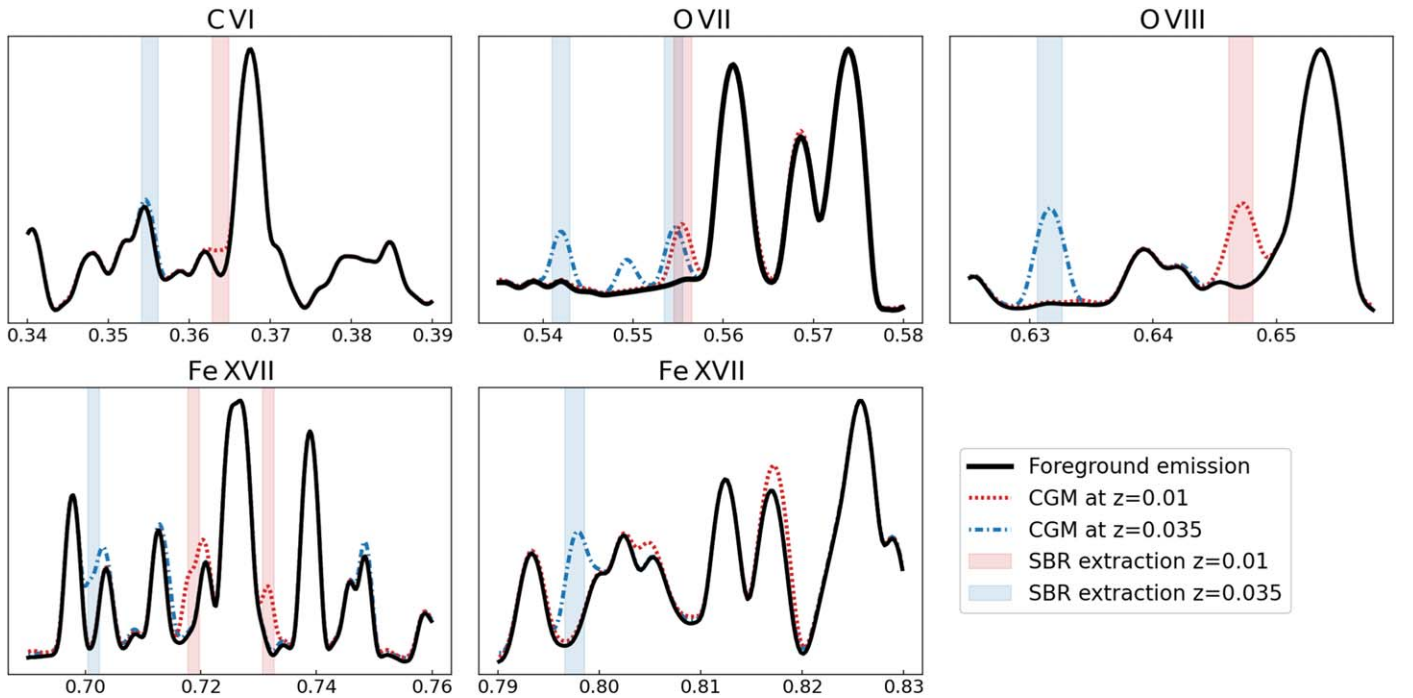
Figure 3. Illustration of the spectral windows used for the surface brightness extraction (see Table 3). The x-axes of the panels are in kiloelectronvolts, and the flux on the y-axes is in arbitrary units. The black lines show a spectral model of the total background, i.e., the MW foreground and CXB emission. We show the thermal emission with arbitrary normalization (to highlight the locations of lines) with a thermal model at 0.2 keV, marked by the blue and red lines for $z = 0.035$ and $z = 0.01$, respectively. The small windows marked by the colored bars are used to distinguish the CGM from the foreground emission.

of a microcalorimeter. The various metal species are independent of each other, allowing a consistent modeling of gas with arbitrary metal abundance patterns.

However, we neglect the effects of resonant scattering from the hot ISM gas in the galaxy (Nelson et al. 2023). We place the low- and medium-mass samples at a nearby redshift of $z = 0.01$, which separates the forbidden O VII line, the C VI line, the O VIII line, and the 725 and 739 eV Fe XVII lines from the MW foreground. However, the O VII resonance line is blended with the MW foreground forbidden line. The extent of the low- and medium-mass halos (R_{500}) fits well within the assumed FoV of the detector. However, since galaxies in the high-mass sample are too large to fit in the 32×32 arcmin^2 FoV, we chose to place these galaxies at $z = 0.035$. This allows us to include the resonance line of O VII, but blends the 739 eV Fe XVII line with MW foreground (see Figure 3).

The Galactic foreground emission is assumed to consist of a thermal component for the LHB (temperature 0.1 keV—McCammon et al. 2002), an absorbed thermal model to account for Galactic halo emission (GHE; temperature of 0.23 keV—McCammon et al. 2002; and a velocity broadening of 100 km s^{-1}), and the North Polar Spur (NPS) or hotter halo component (temperature 0.7 keV—see Das et al. 2019b; Bluem et al. 2022; also broadened by 100 km s^{-1}). Each thermal component is implemented with the APEC model (Foster et al. 2018) with solar abundances (Anders & Grevesse 1989), and the absorption with the tbabs model (Wilms et al. 2000) with a hydrogen column density of 1.8×10^{20} cm^{-2}. The normalizations are $\mathcal{N}_{\mathrm{LHB}} = 1.7 \times 10^{-6}$ cm^{-5} arcmin^{-2} for the LHB, $\mathcal{N}_{\mathrm{GHE}} = 0.43 \, \mathcal{N}_{\mathrm{LHB}}$ for the GHE, and $\mathcal{N}_{\mathrm{NPS}} = 0.05 \, \mathcal{N}_{\mathrm{LHB}}$ for the NPS. The spatial distributions are flat in the mock event files.

The astrophysical background contains unresolved X-ray point sources, mostly distant AGNs (CXB). On average, the flux

distribution of a source follows a power law $S_\nu \propto \nu^{-2}$ (De Luca & Molendi 2004; Hickox & Markevitch 2006) and the $\log N-\log S$ distribution from Lehmer et al. (2012). The average power-law normalization is 4.1×10^{-7} pht s^{-1} keV^{-1} cm^{-2} arcmin^{-2} after excising the brightest 50 point sources from the event file, which make up half of the total CXB flux (and about 3% of the FoV area).

Considerations on the particle background based on Athena X-IFU (Barret et al. 2013, 2018) studies showed that a spectral component due to Galactic cosmic rays will be a factor of 30 to 60 lower than the second-lowest component, the CXB. We included a conservative estimate on the residual particle background, after anticoincidence filtering, of 1 cts s^{-1} keV^{-1} for the FoV. The particle background is assumed to have a flat spectrum and no spatial features. Our mock event files include all the abovementioned components and simulate a 1 Ms observation.

2.3. Analysis

The analysis of the mock event files relies partly on existing software, such as CIAO, but most routines are reimplemented in Python using *astropy* (The Astropy Collaboration et al. 2013, 2018) and the *scipy* packages.

2.3.1. Preparation

While the pixel size of a LEM-like detector array is 15″, the optics and mirror assembly reach a spatial resolution of 10″, which will be utilized through Lissajous dithering. Therefore, we oversample the detector pixels by a factor of 2 for all images that are produced, e.g., for point-source detection. To start the analysis of the simulated event files, we visually inspect the images and spectra around the O VII(f) emission line, determine the redshift by locating the peak of the emission
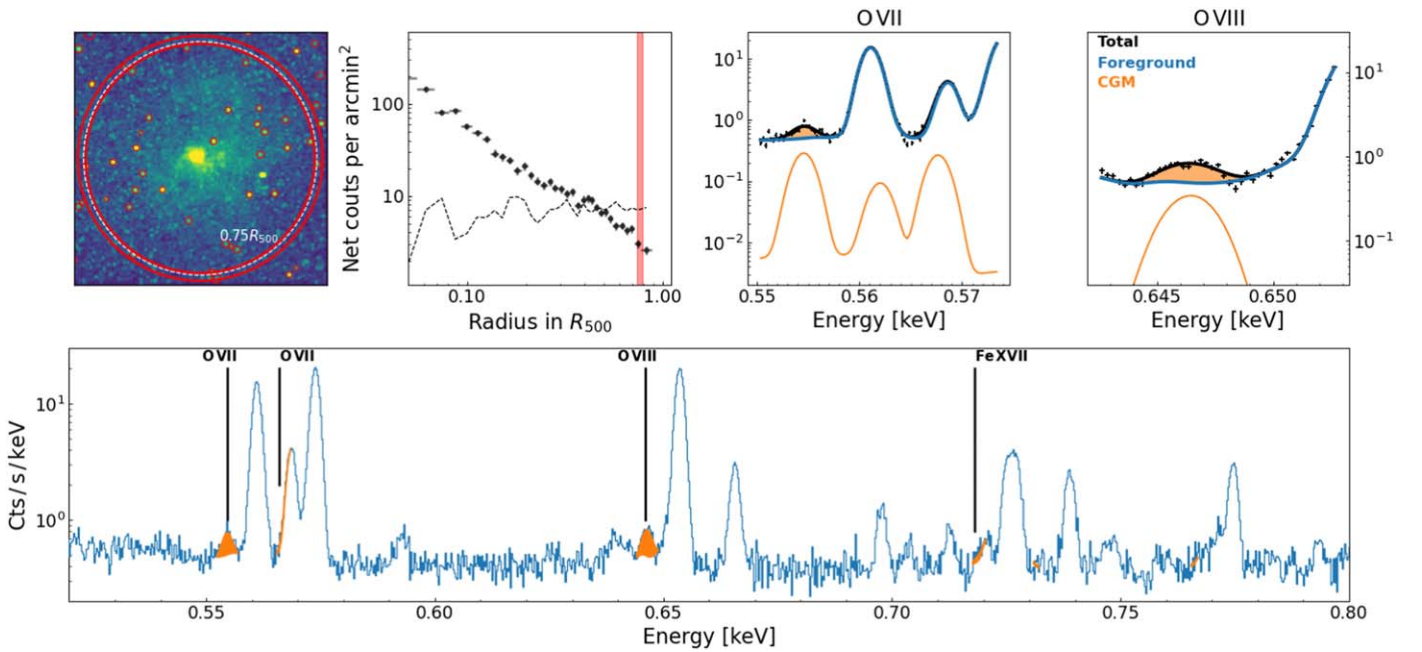
Figure 4. Example for a $10^{11.18}\,M_\odot$ stellar mass galaxy with $R_{500} = 243$ kpc (TNG50, ID 358608, at $z = 0.01$). A map of the narrowband O VIII emission (including background/foreground) is shown in the top left panel, where all the detected point sources are marked by small red circles, and the extraction region used for the other panels is shown as a large red annulus around the 0.75 R_{500} marker. A surface brightness profile of the O VIII line is shown in the second to right top panel, with the spectral region of both, the O VII and VIII emission including the MW foreground, being shown in the two top left panels. A wider spectrum is shown in the bottom panel, with the CGM emission in excess of the foreground/background emission as the orange shaded area.

line, and extract the line surface brightness ± 2 eV around the O VII(f) line. We use the surface brightness distribution to calculate the emission-weighted centroid, which is used as the center of our profiles.

2.3.2. Point Sources

Following these initial tasks, we use the `wavdetect` algorithm included in the CIAO 4.14 package (Fruscione et al. 2006) to detect point sources from the CXB in the observation and in the corresponding background file. Since the point sources are expected to have a continuum power-law spectrum, we use a broadband image, 250–950 eV, for the detection. While several hundred point sources are typically detected, we select the 50 most significant and brightest sources, which contribute about 50% to the total CXB flux, but only cover about 2%–3% of the detector area. The least significant of the top 50 sources is still detected at 100σ. Examples of the detected sources can be seen in the top left panel of Figure 4. The area of these 50 point sources is masked out in the observation and background event file for the following analysis steps. More details on the point-source contribution are given in Appendix A.1.

2.3.3. Surface Brightness Profiles

Our goal is to quantify the CGM emission out to large radii for galaxies in our three subsamples (see Section 2.2.2). The surface brightness profiles of the bright emission lines (see the "Line Photometry" column in Table 3) allow us to understand the structure of the CGM as a function of radius. Therefore, we extract for each line the counts from the mock event files around the previously defined emission-weighted center. We use narrow 2 eV spectral windows centered at the redshifted line energies. The 2 eV spectral window is the optimal width in terms of S/N, and it includes 76% of the line counts. Figure 3

Table 3
CGM Emission Lines Used throughout This Work

Element	Energy (eV)	Peak kT (keV)	Line Photometry $z = 0.01$	0.035	Spectral Analysis
C VI	367.5	0.11	✓	✓	✗
O VII (f)	561.0	0.17	✓	✓	✓
O VII (i)	568.6	0.17	✗	✗	✓
O VII (r)	574.0	0.17	✗	✓	✓
O VIII	653.7	0.27	✓	✓	✓
Fe XVII	725.1	0.43	✓	✓	✓
Fe XVII	727.0	0.43	✓	✓	✓
Fe XVII	739.0	0.43	✓	✗	✓
Fe XVII	825.8	0.54	✗	✓	✓

Note. The peak temperature for each transition is the plasma temperature at which the excitation rate is maximum, assuming CIE. However, this number is for information only, since we include effects such as photoionization in our simulations.

shows the redshifted spectral extraction with respect to the foreground emission for several interesting line windows considered here. The red shaded regions correspond to the extraction for the nearby ($z = 0.01$) galaxies, the blue shaded regions to the more distant ($z = 0.035$) galaxies. In the case of O VII, we can use the forbidden and resonant lines at $z = 0.035$, while for the nearby galaxies at $z = 0.01$, we only use the forbidden line. For Fe XVII, we coadd the three lines, 725, 727, and 739 eV, at lower redshift ($z = 0.01$), while at $z = 0.035$, we use the 725, 727, and the 826 eV lines.

For the surface brightness profiles, we determine the width of the radial bins (annuli) to achieve: (a) a minimum S/N of 3; and (b) a minimum source-to-background ratio of 10%. While (a) limits our statistical uncertainties, (b) prevents systematics in the background from biasing our result. We estimate the background counts based on a simulated blank-field

observation with only foreground and CXB background components, where we repeat the same steps that were performed for the CGM observation, in particular the point-source detection, as this field has a different realization of the CXB point sources. The background counts are estimated in the same narrow bands, but from the whole FoV (minus the excised point sources), to reduce the statistical uncertainty in the background. Since this background estimate assumes an FoV-averaged residual CXB contribution (point sources that are fainter than the 50 brightest that are excluded), we introduce a scaling factor to the background counts in each annulus, based on the broadband emission (±200 eV around the line) of the continuum CXB sources (see Appendix A.2 for details).

To combine the results from all individual galaxy profiles of the various subsamples, we build a median (not stacked) profile, where we take the median surface brightness at each radius and use the 68% scatter among the profiles of our subsample to represent the galaxy-to-galaxy variation.

2.3.4. Structural Clumping in the Gas

While the radial surface brightness profiles demonstrate our ability to detect the CGM to large distances, they do not quantify the level of substructure present in the gas at a given radius, nor do they show how well an X-ray microcalorimeter can detect/characterize the substructure. It is expected that different feedback mechanisms will leave imprints in the CGM. Stellar feedback is able to expel gas from the inner region near the disk to larger radii and cause not only metal enrichment, but also an observable anisotropic distribution of structure within the gas (Péroux et al. 2020; Truong et al. 2021; Nica et al. 2022), especially within intermediate radii ($\sim0.5R_{500}$). A very dominant central AGN will have a major impact on the halo gas distribution. After several feedback cycles, it is expected that the gas distribution will be smoothed by the impact of the AGN.

To capture this information from our mock observations, we divide each galaxy azimuthally into sectors, for which we compute the surface brightness of the emission lines. The ratio between the mean and median surface brightness of all the sectors traces the asymmetry and clumpiness of the X-ray gas (approximated by the ratio of the average squared density to the square of the average density; e.g., Nagai & Lau 2011),

$$\mathcal{C}(r) = \frac{\langle\rho^2\rangle}{\langle\rho\rangle^2} \approx \frac{S_{\mathrm{mean}}(r)}{S_{\mathrm{median}}(r)} , \tag{1}$$

where ρ is the gas density. We note that $\mathcal{C}(r)$ is also known as the emissivity bias in the literature (Eckert et al. 2015). Typical values from observations range from 1, meaning no azimuthal asymmetry or substructure, to about 2 at large radii. Emission from a single line is more prone to vary, due to temperature variations in the gas. We calculate $\mathcal{C}$ in annuli of width $0.25R_{500}$ from stacked images of the O VII(f), O VIII, C VI, and Fe XVII 725 eV lines. This combines forbidden and resonant lines, and the latter are more sensitive to geometry. As Nelson et al. (2023) point out, the O VIII line is only very mildly sensitive to resonant scattering. We combine the signal from these emission lines, which also increases the S/N. We trace the substructure out to a radius of R_{500} (four radial bins), while using eight sectors (45° each). We then stack the $\mathcal{C}$ profiles for galaxies to derive the median profile. We notice that, especially

for lower-mass halos, the scatter in $\mathcal{C}$ is substantial. Since we are only interested in the type of galaxy where $\mathcal{C}$ is significantly larger than 1, we use the range of $\mathcal{C}$ values in the 50th–75th percentile as a diagnostic.

2.3.5. Spectral Analysis

Besides the line photometry to measure the extent and distribution of the CGM, a large-grasp microcalorimeter can also map the dynamical, thermal, and chemical structure of the CGM by analyzing the spectrum. This provides insights on gas motion, outflows, enrichment history, and the dominant reheating process. For example, we can use the signal of the various emission lines to constrain the CGM temperature, abundance ratios, and line-of-sight (LOS) velocity. To avoid fitting all spectral features within the instrument bandpass, we decide to constrain the main properties by focusing on the most important emission lines. We fit a model, which includes background and foreground components, in small (8 eV) spectral windows around the emission lines (Table 3).

For the spectral mapping, we choose the region size based on the brightness distribution of the three lines O VII(f), O VIII, and Fe XVII through an adaptive binning technique (see O'Sullivan et al. 2013; Kim et al. 2019), which we briefly describe here. At every pixel of the combined line image, we derive a radius at which we reach a threshold S/N. This radius can be different for neighboring pixels. The spectral extraction region for each pixel is given by the determined radius. As a consequence, the spectra of neighboring pixels are not independent, and we will oversample the map. We use an S/N of 10 as a threshold parameter, and we do not include pixels if the radius has to be larger than 7′.

We assume the foreground model and CXB models are not known a priori and constrain their parameters through spectral fitting of a separate background spectrum. This background spectrum is extracted from the same observation, using a region outside the central 15′ radius, and we remove bright regions from the galaxy CGM and exclude point sources. This leaves about 30% of the detector area for the background spectrum, which is enough to measure all parameters (temperatures and normalizations of the LHB, GHE, NPS, and CXB) with high precision. The spectral extraction is done using the CIAO tools dmextract and dmgroup, to have a grouped spectrum file with at least one count per bin.

For the spectral fitting, we use Sherpa (Freeman et al. 2001; Burke et al. 2020), which is distributed with CIAO and also provides the Xspec models, such as APEC and tbabs (Arnaud 1996; Foster et al. 2012). We model the background/foreground emission with two absorbed APEC models (GHE and NPS, including thermal and velocity broadening with a velocity of 100 km s^{-1}) and one unabsorbed APEC model (LHB) plus one absorbed power law (CXB) to fit the background components in the mock observations (see Section 2.2). The contamination of the background spectrum with CGM emission of the targeted galaxy is small, since we use a large radius for spectral extraction. However, to account for residual contamination, we add a CGM component to the background spectral fitting as well. The parameters of this CGM component are not used later on. We are able to reproduce the input background parameters within 2% relative accuracy.

For the spectral fitting of the actual CGM regions (determined through our adaptive binning), we apply the

previously determined background parameters and freeze these values. We only leave the CXB power-law normalization free to vary, since each spectral region can contain a slightly different population of CXB sources, while the CXB normalization from the background spectrum is just the average over a larger area.

Our CGM emission model consists of 19 absorbed components: the individual elements C, N, O, Ne, Mg, Si, S, Fe, plus a model for all other elements, one component for each element that includes the effect of the resonant scatter of the cosmic microwave background (Ferland et al. 2017; Khabibullin & Churazov 2019), and one component for the emission from plasma without metals. The normalization of the resonant-scattered components is frozen to half the normalization of the corresponding element, since we removed about half the flux from CXB emission through the point-source masking. Each CGM component has a temperature, redshift, and intrinsic hydrogen density (for the photoionization). We link the temperature, redshift, and density between the elements, as each chemical element has its own emission model component. In order to account for the velocity broadening of the CGM model components, we apply a Gaussian smoothing kernel (xspec gsmooth, with $\alpha = 1$) to the CGM model before convolution with the instrumental response matrix. Furthermore, we note that photoionization is mostly unimportant for the regions (within $\sim 0.8 R_{500}$) and masses considered here (see Appendix B), and therefore we do not leave the density free to vary. We use Cash statistics (Cash 1979) for the fitting of the input spectrum.

As mentioned before, we do not use a broad band of the spectrum, but rather select 8 eV narrow spectral windows centered on the 11 interesting CGM lines listed in Table 3. The reduced χ^2 values are typically very close to 1. After the best-fit parameters are found, we use the Markov Chain Monte Carlo sampling method integrated into Sherpa to find the parameter uncertainties using the Metropolis Hastings algorithm.

3. Results

The results of our analysis demonstrate the extraordinary capabilities of a large-grasp X-ray microcalorimeter for detecting and characterizing the CGM. As an example, we show in Figure 4 the line emission image, surface brightness profile, and spectra for a TNG50 galaxy at the upper-mass end ($\log_{10} M_\star/M_\odot = 11.18$ and $R_{500} = 243$ kpc) at $z = 0.01$. The same galaxy is also analyzed in detail in Section 3.4 using temperature, velocity, and abundance ratio maps. However, we note that typical galaxies of the low- and medium-mass samples will be fainter.

Figure 4 illustrates the power of a LEM-like mission to probe the CGM properties to large radial distances. We illustrate this capability by focusing on a narrow annulus at $0.75 R_{500}$. The top left panel shows the combined image of O VII, O VIII, and Fe XVII, which fills the FoV. The red annulus shows the extraction region that has a 1′ width. The panel to the right shows the surface brightness profile and the background level (dashed line). At the red shaded extraction region, which is the same as in the first panel, the CGM emission still reaches 50% of the background. The other panels show spectra extracted from the same region and highlight the CGM model (orange) over the foreground emission (blue). The two top right panels show close-ups of the spectral region around the O VII triplet and the O VIII line, while the bottom panel shows the spectrum from 544–800 eV with the prominent CGM emission lines indicated.

In Figure 5, we exhibit the imaging capabilities and highlight the superiority of a high-spectral-resolution microcalorimeter over an otherwise equivalent CCD imaging X-ray instrument for CGM science. For the two TNG100 galaxies shown in the panels (the left is an MW-like galaxy at $z = 0.01$, while the right is a high-mass galaxy at $z = 0.035$), we select narrow spectral bands for imaging (O VII or O VIII and Fe XVII; bottom panels). The top left quadrant of each panel shows a broadband image (0.3–2 keV) where only the core of the galaxy is visible. An optical r-band image (the top right quadrant of each panel) shows the distribution of stellar light, which is much smaller than the X-ray CGM emission (black contours). To quantitatively understand how far the emission can be traced, we analyze the median line surface brightness profiles.

3.1. Line Surface Brightness Profiles

We extract surface brightness profiles of four important emission-line complexes: C VI, O VII, O VIII, and Fe XVII (see also Table 3). The profiles are extracted in a 2 eV window around the redshifted line energy, which minimizes the contamination with foreground lines from the MW. We extract a profile of a simulated background/foreground observation in the same way and subtract this from the observation of the CGM.

Each of the low-, medium-, and high-mass samples contains 40 galaxies, while the former two have the galaxies at $z = 0.01$ and the latter at $z = 0.035$. Details of the individual galaxies, such as stellar mas, gas mass, and black hole mass, are given in Tables 2, 4, 5, and 6.

We analyze the median profile with the radius scaled by R_{500}. Within each sample (low-/medium-/high-mass), we use the 33rd and 66th percentiles of the SFRs as thresholds to subdivide further. We therefore have nine (sub)samples, three star formation samples per mass, which all comprise either 13 or 14 galaxies.

We conservatively consider CGM detection if the measured signal is at least 10% of the background and the S/N of each extracted radial bin is at least 3. We show profiles in Figures 6, 7, and 8 for EAGLE, TNG100, and Simba, respectively. The low-mass, medium-mass, and high-mass samples are shown in blue, orange, and green, respectively. The subsamples are shown with solid, dotted, and dashed lines for the top, lowest, and intermediate thirds, respectively. Therefore, each line is the median profile of 13 or 14 galaxies. The typical 68% scatter is shown for the star-forming, medium-mass sample as the orange shaded region.

We detect the C VI, O VII, O VIII, and Fe XVII lines in emission in all simulations. Based on the galaxy mass, all simulations detect the CGM emission out to R_{500}. Simba is clearly the faintest. However, there is significant scatter between the galaxies of a single simulation, and between the different simulations. O VIII can be detected out to $R_{200} \approx 1.5 R_{500}$ ($M_{200} \approx 1.35 M_{500}$) for the more massive galaxies in TNG100 and EAGLE, and out to R_{500} in Simba. The other lines that we tested are basically undetected in Simba for the high- and low-mass samples.

The O VIII is the brightest line, with the highest number of counts and a relatively low background, followed by O VII and Fe XVII. While C VI can be detected in most galaxies, it is very
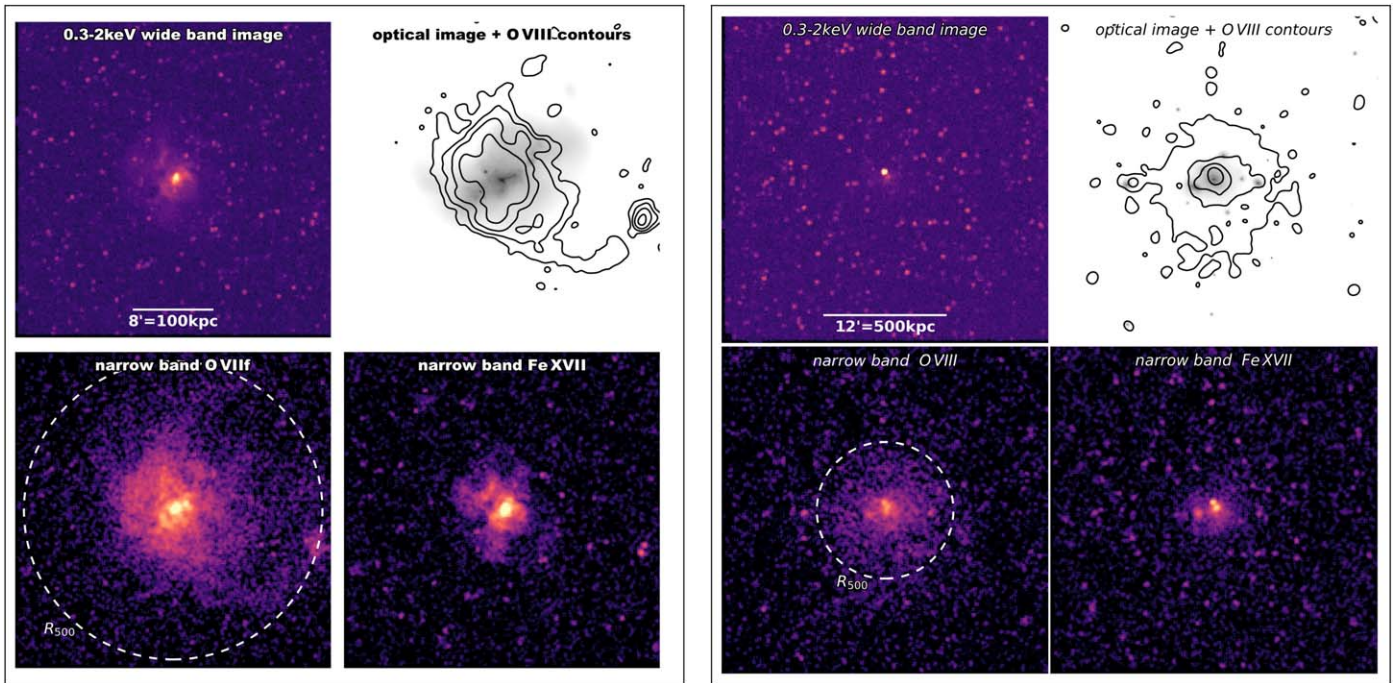
Figure 5. Illustrating the capabilities of a LEM-like mission for mapping the CGM. Left: galaxy halo of the size of the MW at $z = 0.01$ (TNG100, ID 417281). Right: high-mass galaxy at $z = 0.035$ (TNG100, ID 337444). The four panels in each image show the broadband image similar to a CCD-resolution instrument (top left), the optical r-band image with O VIII contours (top right), the O VII(f) or O VIII image with R_{500} indicated (bottom left), and the Fe XVII image (bottom right).

weak in Simba. For the oxygen and carbon, TNG100 and EAGLE are comparable, but TNG100 typically has a steeper shape, leading to a smaller detection radius. Especially for galaxies in the low- and medium-mass sample (blue and orange), TNG100 has a clear trend that galaxies with higher SFRs are also brighter (the solid line above the dashed line, with the dotted line being lowest). This has also been pointed out, e.g., by Oppenheimer et al. (2020). The lowest-mass galaxies with little star formation appear very faint in EAGLE. However, for the medium-mass sample, we only partially find the same trend with SFR (the solid line is highest, but the dotted and dashed lines are comparable). For the high-mass sample, we find in both TNG100 and EAGLE that at larger radii close to R_{500}, the brightness is independent of the SFR (see also Oppenheimer et al. 2020).

The medium-mass sample shows oxygen and iron emission at about 0.6–1 R_{500} in both simulations, EAGLE and TNG. For C VI, we find a big difference between EAGLE and TNG100, where in EAGLE carbon is detected out to 0.8 R_{500} and in TNG100 only to about 0.3 R_{500}. The difference in the visibility of C VI between EAGLE and TNG100, at higher halo mass, is not explained by the higher EAGLE CGM temperatures, but possibly by a different metal composition, as carbon is produced also by AGB stars. The visibility of the high-mass galaxies placed at $z = 0.035$ is not limited by the FoV and can therefore be traced far beyond R_{500}, as in the case of O VII (both resonant and forbidden lines combined; see Figure 3) and O VIII. We also can detect Fe XVII in both EAGLE and TNG100, nearly to R_{500}, depending on the SFR. C VI was not detected in the high-mass TNG100 galaxies, but it is very clearly visible in EAGLE.

Clearly, Fe XVII is detected best in EAGLE, likely because some of the galaxy halos are hotter. Comparing the scatter between the galaxy halos of a given sample, we notice a slightly larger scatter among the TNG100 galaxies. The scatter

of the CGM profiles between the Simba galaxies can only be measured at smaller radii.

3.2. Emission-line Ratios

If the hot gas in and around galaxies is not isothermal, we expect the emission-line ratio profiles to reflect any deviations from the isothermalities of the gas, because of the sensitivity of the emission to gas temperature. In the simplest case of a constant (with radius) abundance of heavy elements, and in the limit of collisional ionization equilibrium (CIE), we expect the Fe XVII lines to become stronger relative to the O VII lines, if the temperature increases with radius (see Table 3). In the case of the same element (e.g., oxygen), the line ratio, e.g., O VII and O VIII, is proportional to the gas temperature. At large radii with low gas densities, photoionization becomes important and changes the line ratios. We have quantified this transition in Appendix B. In our default analysis, we coadd the O VII(f) and O VII(r) for the high-mass samples (i.e., at $z = 0.035$) to increase the signal. We also show in Appendix B that the typical densities of these higher-mass halos do not show the biasing effects of photoionization. Therefore, using both O VII lines for higher-mass halos to infer temperature does not create a bias. However, the line ratios cannot be compared to the $z = 0.01$ samples, where only O VII(f) is used. When comparing the emission lines of different elements (e.g., C VI and Fe XVII), the conclusions are less clear, since not only does the temperature change in the gas, but the enrichment mechanisms also differ: SNe Ia contribute significantly to the abundance of iron, but not to that of carbon or oxygen.

Figure 9 shows the O VII-to-O VIII line ratio for the same samples that were shown in Section 3.1. Looking at the nearby galaxies in Figure 9 (left), we notice a systematic offset between star-forming TNG100 and EAGLE galaxies (the solid blue and orange lines), where the EAGLE ratios are always
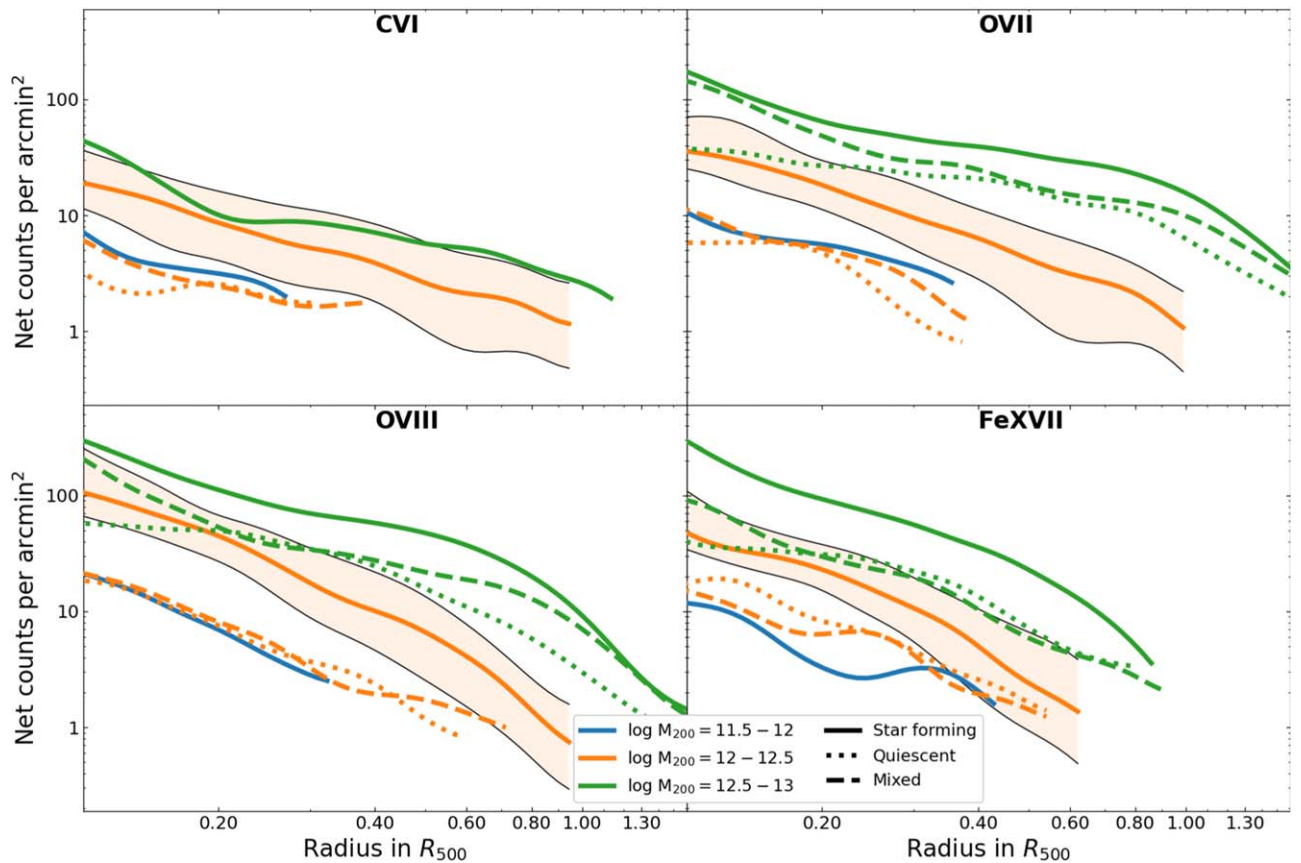
Figure 6. Median profiles of the CGM emission from the EAGLE galaxies, binned by halo mass (M_{200}). The solid, dotted, and dashed lines correspond to the star-forming, quiescent, and mixed subsamples, respectively. The blue, orange, and green curves show the low-, medium-, and high-mass galaxy halos, respectively. The orange shaded region represents the 68% scatter, shown only for star-forming, medium-mass galaxies for visibility purposes.

below the TNG100 ones. This indicates that the EAGLE galaxy halos are systematically hotter within the covered radius $<0.5R_{500}$ (see also Truong et al. 2023). For the mixed star-forming galaxies (33rd to 66th percentile of SFRs), we find comparable line ratios within the scatter among TNG100 and EAGLE, while the Simba halos have lower line ratios (see also Truong et al. 2023). Unfortunately, statistics only allow us to derive line ratios to about $0.4\,R_{500}$, until which we see a rising line ratio, indicating a hotter core and cooler outer regions (Figure 9). For the high-mass galaxy halos (Figure 9, right), we see a similar trend of star-forming galaxies being hotter in EAGLE with respect to TNG100 and Simba (a lower O VII-to-O VIII ratio). The TNG100 halos appear almost isothermal (a constant line ratio), while the EAGLE galaxies have an increasing line ratio toward the outer regions and become even steeper beyond $0.6\,R_{500}$. At these large radii, the difference between star-forming and quiescent galaxies appears to vanish: the impact of star formation is most prominent in the core. In principle, we need to include the effects of photoionization in our interpretation of line ratios at large radii, since at very low plasma densities the assumption of CIE is no longer applicable. However, simulating several line ratios with fixed plasma temperature and only changing the density showed that above a density of $3 \times 10^{-5}\,\mathrm{cm}^{-3}$, the changes in the ratio are less than 5%–6%. Densities within R_{500} are expected to be larger than that (e.g., Bogdán et al. 2013b). We note that for regions with column densities above $N_H = 10^{21}\,\mathrm{cm}^{-2}$, the O VII-to-O VIII ratio will be affected by electron-scattering escape (Chakraborty et al. 2020b). However, for a typical high-mass

galaxy ($\log M_{500} \sim 12.5$), column densities are generally below this value.

3.3. Substructure in the CGM Emission

In order to analyze the substructure that can be detected in the mock observations, we apply the method introduced in Section 2.3.4. $\mathcal{C}$ is calculated for the TNG100, EAGLE, and Simba halos in all three mass samples.

As pointed out before, $\mathcal{C} \approx 1$ means that there was no clumping detected, and observations have shown that it can rise up to 2 at R_{500}. This can be associated with the substructure in the outskirts being accreted. For clusters, Eckert et al. (2013, 2015) and Zhuravleva et al. (2015) have observed very low clumping factor values, even at R_{500}, while Simionescu et al. (2011) found higher values for the Perseus cluster.

Since the calculation of the clumping factor of a single emission line, like the O VII, could bias the results due to the sensitivity to temperature changes in the CGM, we use the stacked signal of the O VII, O VIII, and Fe XVII lines, which are all sensitive to different temperatures (Table 3). The combined samples cover a wide range of galaxy halos in terms of mass, SFR, or temperature. Therefore, we divided the sample into galaxies with a central SMBH below the median SMBH mass, and the ones above, shown in Figure 10 as the dark shaded and light shaded regions, respectively.

We find an interesting trend for the black hole mass distinction. We do not see any difference in EAGLE for different SMBH masses (all values outside the core are within
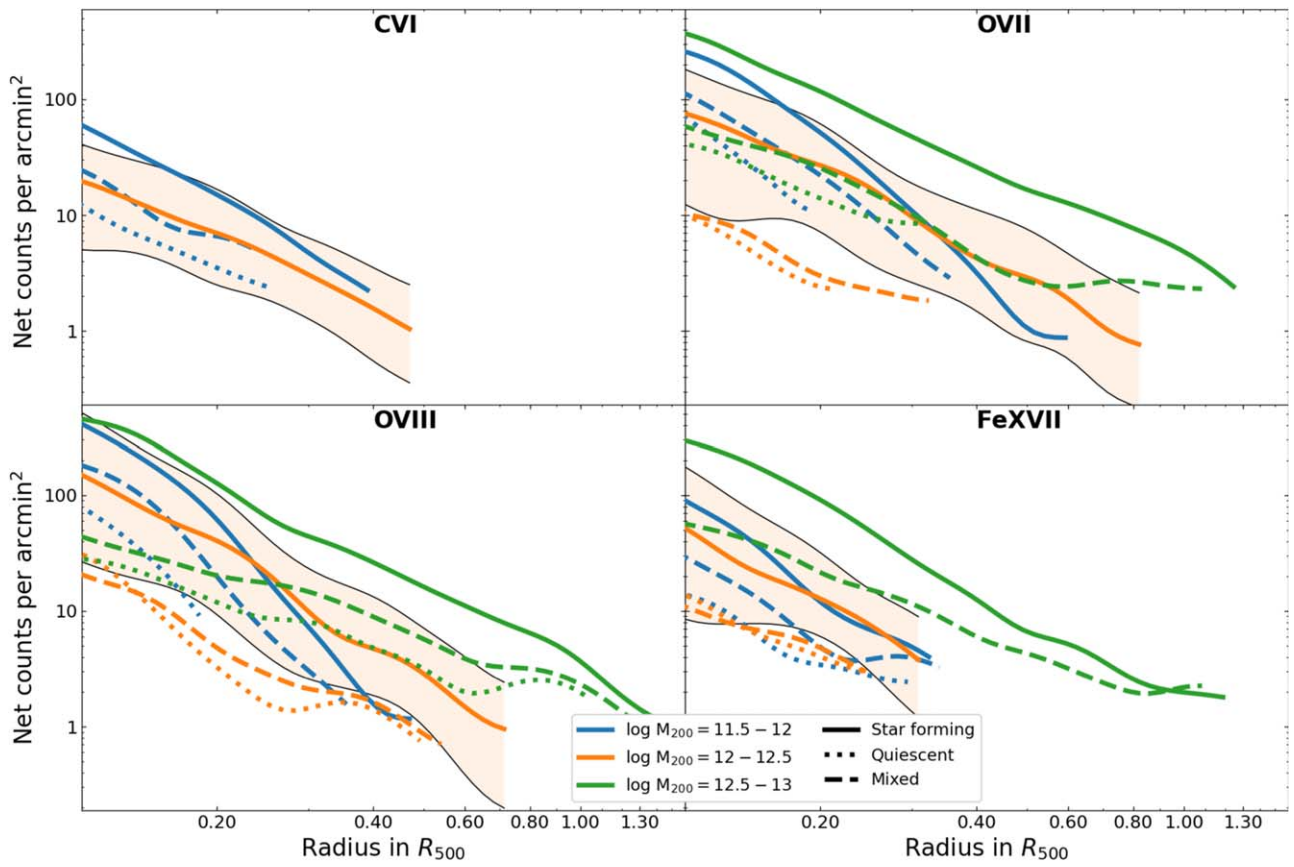
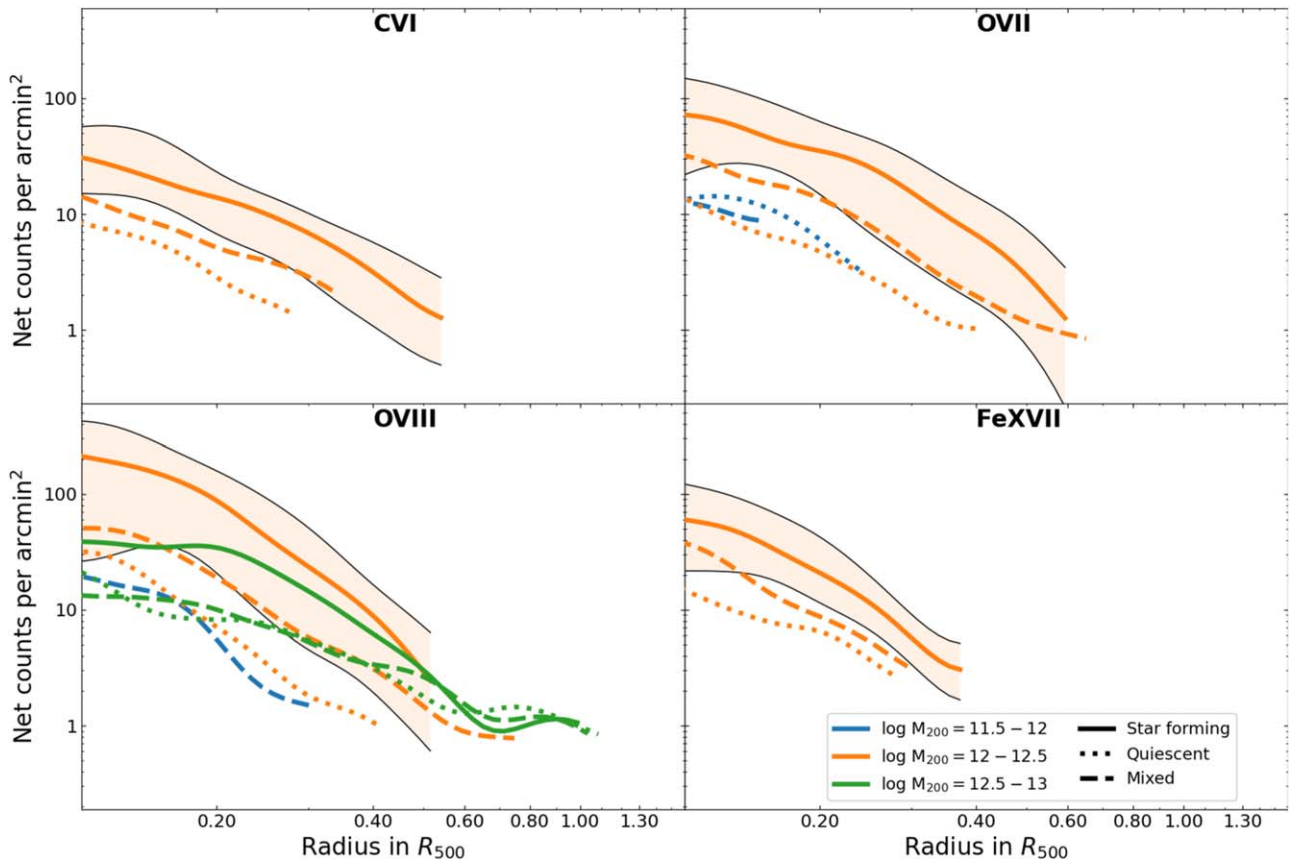**Figure 7.** The same as Figure 6, but for TNG100 galaxy halos.

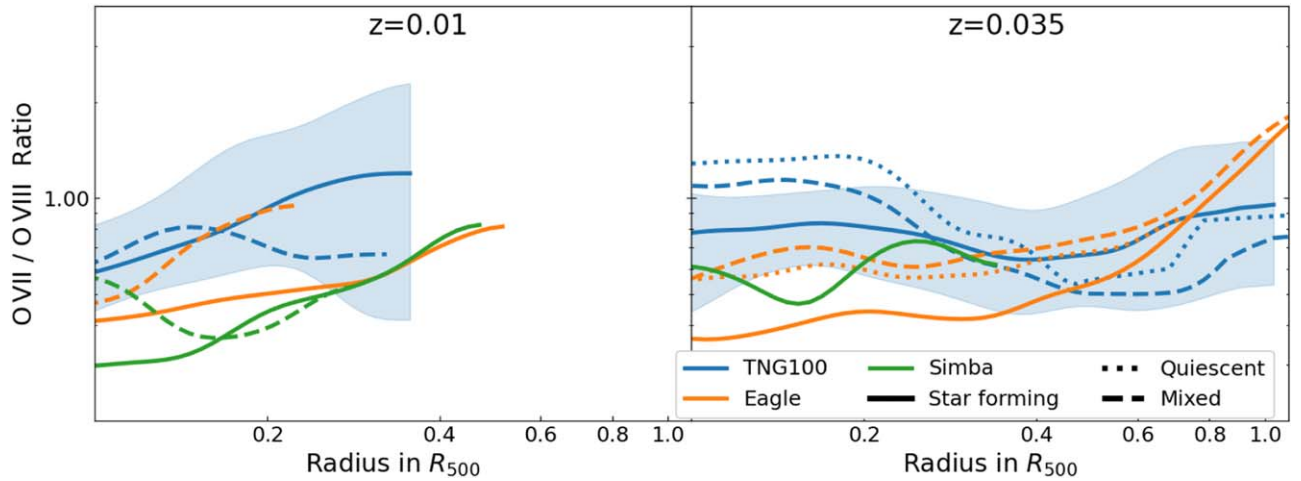**Figure 8.** The same as Figure 6, but for Simba galaxy halos.

Figure 9. The O VII-to-O VIII line ratios for the low- and medium-mass samples (left) and high-mass samples at larger redshift (right). As in the profile plots, the solid, dotted, and dashed lines correspond to star-forming, quiescent, and mixed subsamples, respectively, while the orange curves show EAGLE galaxies, the blue curves TNG100, and the green curves Simba. The blue shaded region represents the 68% scatter, shown only for star-forming TNG100 galaxies for visibility purposes.

1 to 1.1; see Figure 10, middle panel). However, galaxies in TNG100 show a dichotomy (Figure 10, top panel), as we find systematically higher $\mathcal{C}$ for lower SMBH masses outside $0.4R_{500}$, while massive SMBHs show a very similar trend between EAGLE and TNG100. The Simba galaxy halos (Figure 10, bottom panel) are generally fainter and the statistical uncertainties are larger, but lower-mass SMBHs appear similar to the trend in TNG100, as they have higher $\mathcal{C}$, but this is less significant. Recent results from simulations by Planelles et al. (2014, 2017) and Rasia et al. (2014) indicate that SNe, and especially AGN feedback, smooth out the gas distribution and suppress a higher clumping factor. While TNG100 and Simba have efficient AGN feedback prescriptions that increase the gas kinematics, AGN feedback only becomes dominant with higher SMBH masses. We can see this trend in our results (Figure 10, top panel and, less significantly, bottom panel), where higher-mass black holes have more clumping near the core and a smoother gas distribution at larger radii, compared to low-mass black holes. EAGLE instead pressurizes the gas more efficiently, which lowers the impact of the SMBHs on the gas clumping. It should be noted that the numerical schemes, hydrodynamic solvers, and subgrid physics, especially of feedback, in the simulations suites are different, which will impact the gas distributions. A smoothed particle hydrodynamics simulation will also produce a smoother gas distribution (e.g., Rasia et al. 2014).

3.4. Spectral Analysis

The detectability of CGM emission lines with a LEM-like instrument out to large radii offers the opportunity not only to derive one-dimensional profiles, but also to map the emission out to R_{500} and measure temperatures, LOS velocities, and abundance ratios. We described our spectral fitting approach in Section 2.3.5, and we apply it here to two galaxies selected from TNG50 of the IllustrisTNG project (Nelson et al. 2019b; Pillepich et al. 2019). TNG50 provides a higher particle resolution than TNG100 (baryon particles about 16 times smaller in mass and a simulation volume about 10 times smaller), enabling in-depth studies of the velocity structure of individual galaxies. However, we verified that our previous results are not biased by the properties of TNG100 (which

provides a larger volume and larger galaxy samples to select galaxies from). Since we do not want to select a large number of galaxies, but rather to study two examples in more detail, a larger simulation box will not provide any advantage.

We explore two galaxy halos in more detail. The first galaxy (358608) has a halo mass of $10^{12.7}\,M_{\odot}$, which would place it in our high-mass sample. It has a relatively high stellar mass of $10^{11.18}\,M_{\odot}$ and a high SFR, $3.87\,M_{\odot}\,\mathrm{yr}^{-1}$. With a mass of $10^{8.64}\,M_{\odot}$, its central SMBH is relatively dominant, and we expect both AGN and stellar feedback to be present. Placing our galaxy at $z = 0.1$, the galaxy slightly exceeds our FoV ($R_{500} = 243$ kpc, corresponding to $19.7'$).

Figure 11(a) shows the observed (i.e., including background and foreground) O VIII emission. We see a bright core and extended CGM emission out to the edge of the FoV ($16'$ radius or 195 kpc). Brighter filaments extend to the north (forming a rim around a lower-surface-brightness region) and southeast, perpendicular to the galactic disk, which is edge-on and oriented southwest to northeast (see the optical r-band image tracing the stellar population in Figure 11(b)). The optical image also shows a smaller structure, about 100 kpc to the west, which is a smaller galaxy. It also has an X-ray counterpart in the O VIII image. The X-ray brightness in the simulation (Figure 11(c)) shows the "true" distribution of the hot gas, which is very filamentary.

We derive the spectral maps following our strategy laid out in Section 2.3.5. We simultaneously fit the spectrum within 8 eV narrow bands around the emission lines (Table 3) to derive the temperature map of this system (Figure 11(d)). The temperature constraints mostly come from the relative line strengths of the O VII(f), O VIII, and Fe XVII lines and will be most sensitive for tracing the temperature between 0.15 and 0.45 keV. We note that for the majority of regions, the effects of resonant scattering and photoionization are small, and the plasma is close to CIE (see also Appendix B). The typical statistical uncertainties vary between 0.03 and 0.005 keV, so the relative uncertainties range between 1% and 10% (see Figure 11(d)). We note that for regions that are less dense and cooler, the uncertainties will be higher, e.g., at the virial radius and beyond (Bogdan et al. 2023).

Comparing this observed temperature map with the idealized, emission-weighted temperature (0.5–1 keV band)
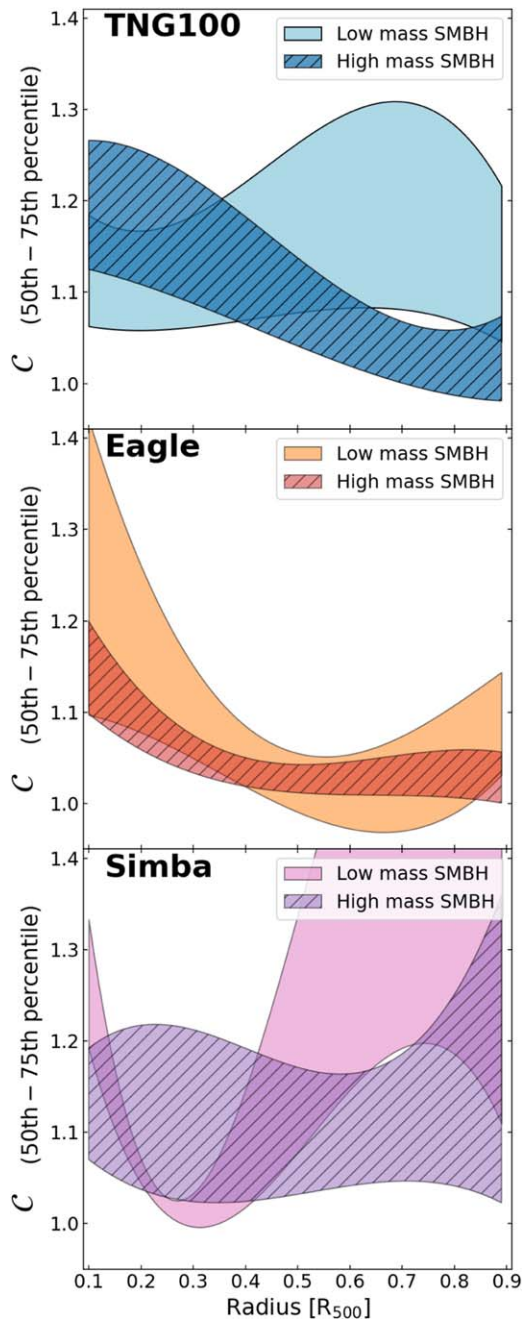
Figure 10. Azimuthal asymmetry as a function of radius, parameterized by the clumping factor $\mathcal{C}$ (defined in Section 2.3.4). We show the 50th–75th percentile of the sample to illustrate the galaxy halos among the sample with high substructure, which are different in TNG100 (left) and EAGLE (right). The darker shaded area is for higher-mass black holes in the galaxy sample, while the lighter shaded area shows low-mass black holes.

derived from the simulation (Figure 11(f)), we can reproduce the brighter parts to the north of the core and the southeast. The emission-weighted temperature is even higher in these regions, mostly because the lines that we used from our mock observation to probe the gas temperature are not sensitive enough to the hotter gas components. We note that a mass-weighted temperature will be biased toward high-mass, low-temperature gas cells, and therefore will be lower than the emission-weighted temperature, which more closely reflects our measured quantity in the mock observations.

For every fitted region, we leave the redshift free to vary during the spectral fit, which is used to derive the LOS velocity information. We note that all the redshifts of the CGM redshift components (emission from the various chemical elements) are linked together in the spectral fit, and we therefore derive a single velocity from all the line centroids. The velocity map (Figure 11(g)) reveals a split between east and west, with an average difference between the two sides of about $300\,\mathrm{km\,s^{-1}}$. As this is most pronounced in the central region, it can be explained by the rotation of the disk. The higher-velocity gas (the red region southeast of the core) is likely an outflow, since it overlaps with the hotter regions. The predicted emission-weighted velocity map from the simulation (Figure 11(i)) confirms this, as it shows structures that are very consistent: the central rotation of the disk, the higher-velocity part to the southeast, and the large-scale velocity structure of the hot gas. A subsequent paper (ZuHone et al. 2023a) will analyze the velocity structure of the simulated galaxy halos in great detail. The statistical uncertainty mainly depends on the number of counts in a line. With our adaptive binning described in Section 2.3.5, we find a velocity uncertainty of about 25–$45\,\mathrm{km\,s^{-1}}$ in the brighter central regions and about $80\,\mathrm{km\,s^{-1}}$ in the lower-surface-brightness region northeast of the center. We assumed conservatively a 2 eV response across the FoV.

We are not constraining individual elemental abundances, since there is a degeneracy with density. There are cases where this degeneracy can be broken, e.g., by observing the CGM line emission and the absorption of a sufficiently bright background AGN by the CGM, the former proportional to the square of the density (emission measure) and the latter proportional to the column density. However, we are able to reliably determine abundance ratios (with respect to solar) and show the observed oxygen-to-iron ratio in Figure 11(j). This abundance ratio is sensitive to the enrichment history, mainly the SNe Ia versus core-collapse SNe ratio (Mernier et al. 2020). We find typical values in the central region $[\mathrm{O/Fe}] = -0.3$ ($Z_\mathrm{O}/Z_\mathrm{Fe} = 0.5$) and values closer to $[\mathrm{O/Fe}] = 0$ ($Z_\mathrm{O}/Z_\mathrm{Fe} = 1$) and above in the outer regions. This is consistent with the predicted O/Fe brightness from the simulation (Figure 11(l)), which shows the center and outflows to be more Fe-rich. For galaxy clusters and groups, the oxygen abundance distribution has been found to be flat, while iron is centrally peaked (Werner et al. 2006; Mernier et al. 2017; Vogelsberger et al. 2018), which leads to an increasing O/Fe profile. A similar trend can be expected for galaxies (Geisler et al. 2007; Segers et al. 2016; Matthee & Schaye 2018). Some regions, especially in the southeast, have very high oxygen abundances, up to 2.5. Typical uncertainties range from 10%–20% in the center to 70% in the faintest regions.

The second galaxy (467415) that we map in detail is also selected from TNG50, but with a lower halo mass of $10^{12.32}\,M_\odot$, which would place it in the medium-mass sample. The stellar mass, $10^{10.94}\,M_\odot$, is relatively high for its size, and the SFR of $8.9\,M_\odot\,\mathrm{yr^{-1}}$ might still dominate its halo environment. Also, its SMBH mass is at the higher end, with $10^{8.33}\,M_\odot$, which makes this another interesting target for studying the effects of stellar and AGN feedback. The radius, $R_{500} = 183\,\mathrm{kpc}$, is within the FoV at $z = 0.01$. The observed O VIII emission (Figure 12(a)) is brightest in the center, but is detected out to almost 100 kpc and some filaments beyond that. The distribution is not azimuthally uniform, but seems to be aligned along filaments, mainly to the southeast, the north, and a narrow region to the west. The r-band contours in
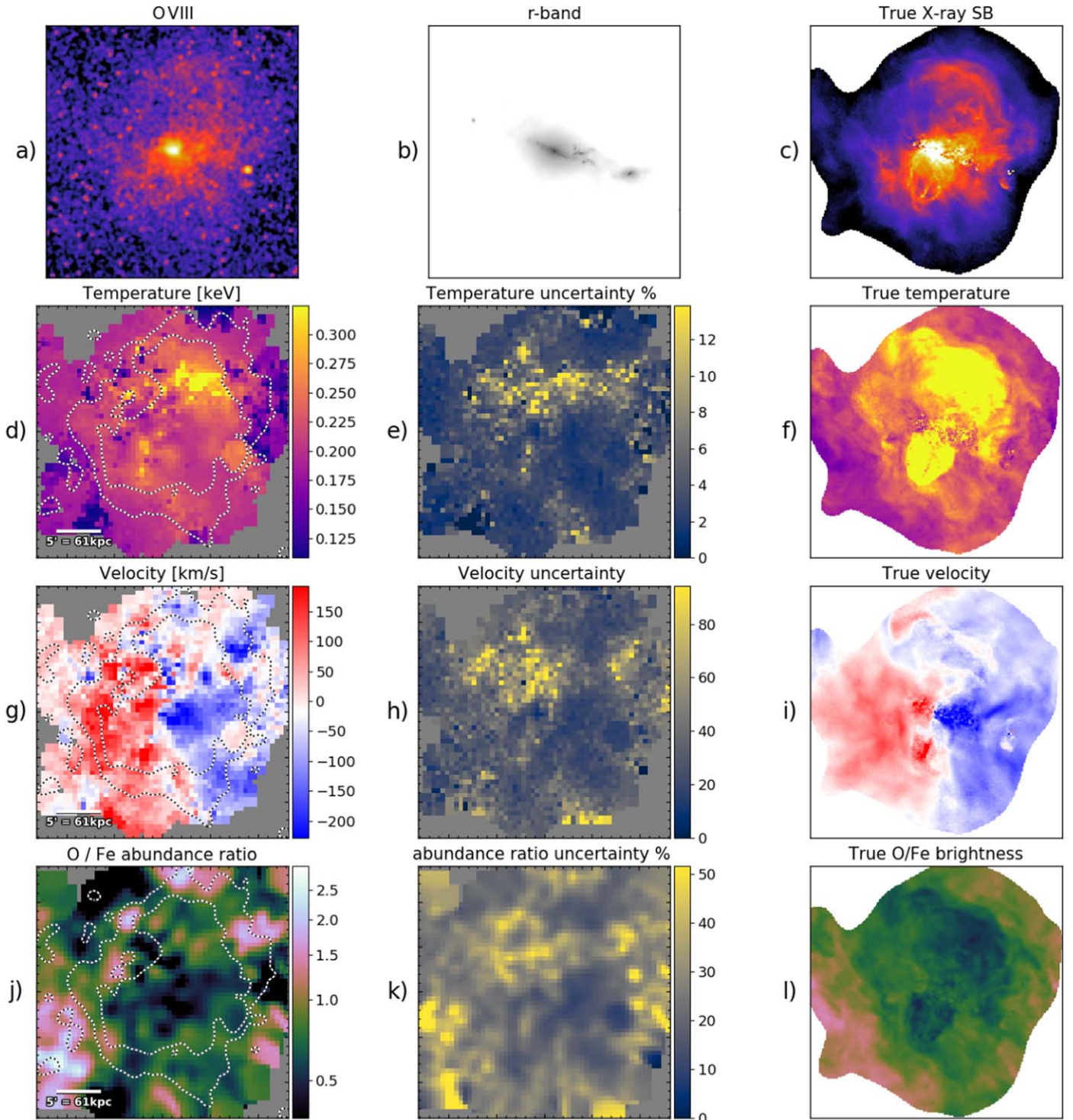
Figure 11. Spectral map of galaxy 358608 from TNG50 (for details, see Section 3.4) showing the observed O VIII surface brightness (a), the predicted optical *r*-band signal (b), the simulated X-ray brightness (c), the observed temperature in keV (d) and error map (e) from a simultaneous fit to O VII, O VIII, and Fe XVII lines, the emission-weighted temperature from the simulation (f), the observed average line velocity shift in km s^{-1} (g) and error map (h), the predicted emission-weighted LOS velocity in the simulation (i), the observed O/Fe abundance ratio (j) and error map (k), and the predicted O/Fe brightness ratio in the simulation (l).

Figure 12(b) show one single galaxy at the center and some much smaller and fainter structures to the south, possibly small satellite galaxies. Figure 12(c) displays the X-ray surface brightness in the simulation.

The observed temperature map (Figure 12(d) and the error map 12 (e)) shows the hottest emission (∼0.3 keV) near the center of the galaxy, while the temperature in the outer filaments drops to 0.18 keV. We identify slightly hotter

structures, extending from the southeast to the northwest, while the northeast-to-southwest axis has cooler gas. The uncertainties are again in the 1%–10% range. The temperatures are broadly consistent with the emission-weighted temperature in the simulation (Figure 12(f)).

The velocity (Figure 12(g) and the error map 12(h)) ranges from 250 km s^{-1} in the southeast to -250 km s^{-1} in the northwest, outside the stellar disk. These are even higher
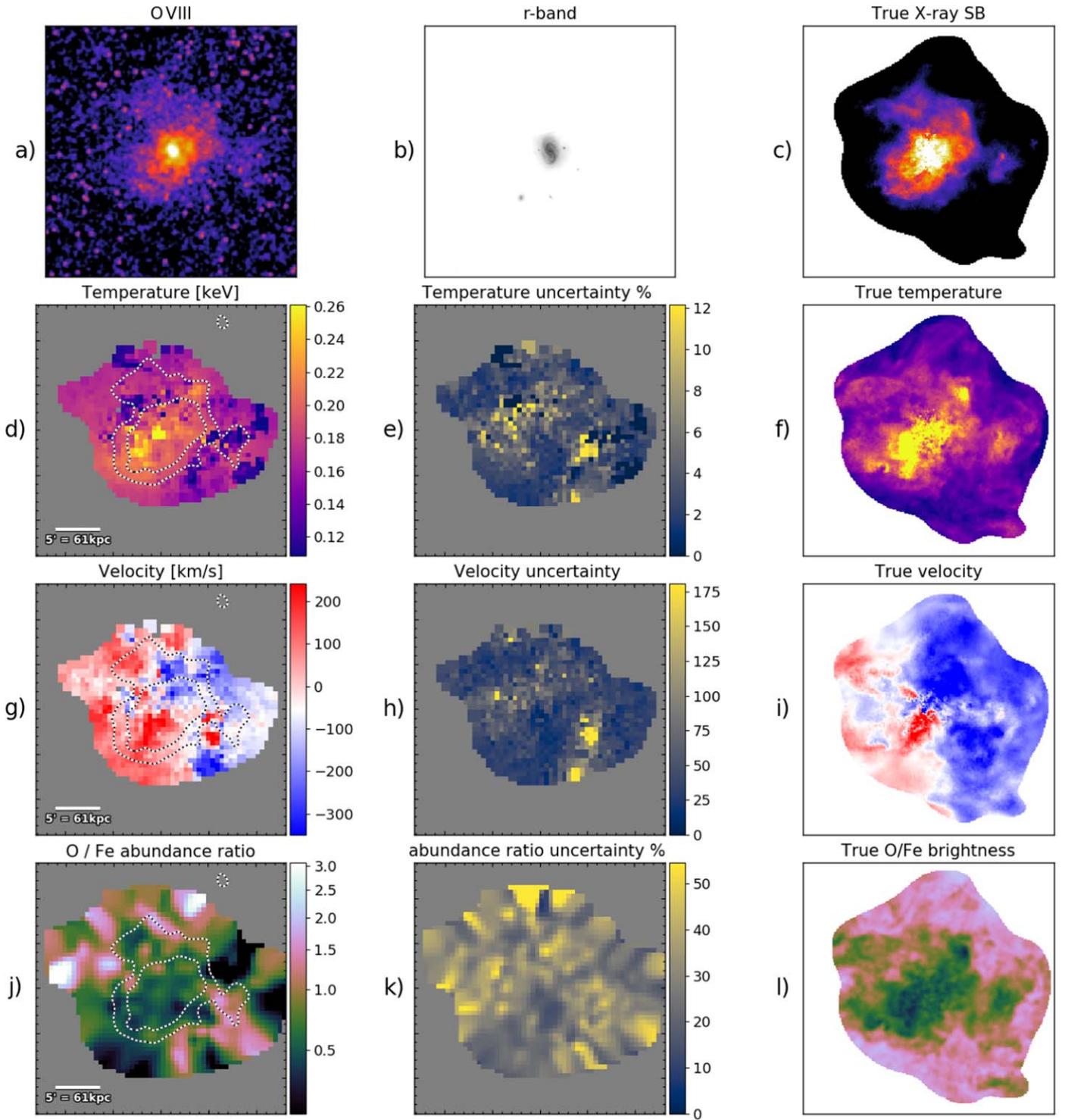
Figure 12. The same as Figure 11, but for the lower-mass galaxy from TNG50 (ID 467415; details in Section 3.4).

velocities than within the first, more massive galaxy. This coincides with the hotter regions on the temperature map and is consistent with the predicted velocity from the simulation (Figure 12(i)). Along the faint, low-temperature regions in the southwest and northeast, the velocities are lower than the surrounding ones. The statistical uncertainties are similar to the other galaxy, ranging from 20 to 80 km s^{-1}.

Last, the oxygen–iron map (Figure 12(j) and the error map 12(k)) has typical values between 0.5 and 1, but also several small regions have ratios well above 1 (statistical uncertainties are between 20% and 70%). This is consistent with the predicted O/Fe brightness in the simulation (Figure 12(l)), where the iron-rich gas is again in the center and along the high-velocity, high-temperature trajectory from the southeast to slightly north of the core.

The level of detail that is revealed in these spectral maps is unprecedented for galaxy-sized halos. Typical spectral maps from CCD-based detectors (e.g., Chandra or XMM-Newton)

can only reach large radii (e.g., R_{500}) for galaxy clusters and massive galaxy groups, but without any LOS velocity information.

4. Discussion

4.1. Tracing the CGM with X-Ray Microcalorimeters

The extended gaseous halos around MW-like galaxies are predicted by simulations and have been detected in stacked broadband images. Constraining their extent, brightness profile, azimuthal distribution, and enrichment with various elements for individual galaxies will allow us to distinguish between simulation models and ultimately enable us to understand the changing feedback processes of galaxies on various scales. The X-ray continuum emission of these galaxies is very faint, but the bright emission lines, namely O VII, O VIII, and Fe XVII, are clearly detectable over the local background and foreground. Selecting a narrow ~2 eV energy band around these lines results in a high-S/N detection with a LEM-like observatory, in a 1 Ms exposure of a $z = 0.01$ galaxy, and even allows the 2D mapping of these galaxy halos. Only focusing on emission lines and not having the continuum information will still allow the majority of science questions to be answered: how is the hot gas distributed and what are the relative metal abundances (e.g., wrt iron)? Only the degeneracy between metallicity and density cannot be easily broken.

The faint CGM line emission around individual, nearby spiral and elliptical galaxies cannot be detected and mapped with current X-ray CCD instruments due to the bright MW foreground. Even state-of-the-art DEPFET detectors such as the Athena/Wide Field Imager (Meidinger et al. 2017), with its ~80 eV energy resolution, will not be able to distinguish the CGM emission lines from the much brighter foreground. A galaxy redshift of at least 0.12 is necessary to shift the O VIII line from the foreground, which will also reduce the apparent size of the galaxy to about $1'$ and the total flux to about 8%, with respect to a galaxy at redshift 0.01.

The development of microcalorimeters marks the start of a new epoch in X-ray astronomy, reaching unprecedented energy resolution while spatially resolving the source structure. The currently planned Athena/X-IFU instrument (Barret et al. 2018) will have a large effective area and good spatial resolution. However, the FoV of $\sim 5 \times 5$ arcmin^2 (before reformulation) is clearly not sufficient to observe the extended CGM of nearby galaxies. At $z = 0.01$, an MW-sized galaxy has $R_{500} \approx 15'$ and therefore requires about 30 pointings. Moving to a higher redshift and utilizing Athena's large effective area can reduce the required amount of observing time to a factor of 5–10 times what a LEM-like mission would need. Galaxies at $z \gg 0.01$ will also not offer the same amount of structure that can be resolved. Since simulations predict the variance between galaxies, also based, e.g., on the SFR, one would like to observe a medium-sized sample of 10–20 galaxies.

The XRISM (Tashiro et al. 2018; successfully launched in 2023) also has a microcalorimeter on board. However, its FoV is limited to only $3' \times 3'$, the effective area is about 10–15 times smaller than LEM, and together with the arcminute spatial resolution and only 6×6 pixels, it will not be able to map the extended CGM.

Other mission concepts with a large-effective-area microcalorimeter include LEM (Kraft et al. 2022) and HUBS (Zhang et al. 2022). While HUBS does not have enough spatial

resolution to map the structure and distinguish X-ray point sources in the field, LEM is clearly optimized to CGM science by having sufficient energy resolution (2 eV), a large effective area similar to XMM-Newton, a $10''$ PSF, and a large FoV of ~900 arcmin^2, allowing one to map nearby galaxies in a single pointing. In contrast to typical X-ray observations of faint, diffuse sources, the instrumental background level plays only a minor role when using a narrow energy band of a microcalorimeter: the requirement for Athena/X-IFU is to reach an internal particle background level of 5×10^{-3} cts s^{-1} cm^{-2} keV^{-1} (Lotti et al. 2021). This should be achieved through a graded anticoincidence shield, while the background is predicted to be about an order of magnitude higher without the shielding. For our results, we conservatively assume a constant particle background level in the soft band of 8.6×10^{-2} cts s^{-1} cm^{-2} keV^{-1}, which is more than 15 times higher than the Athena requirement. The foreground emission, however, scales with the effective area of the mirror. In the case of LEM, it will be the dominant background component, and even at the foreground continuum around the O VIII line, the particle background is still below all other components (foreground and CXB).

4.2. Model Distinction

We have demonstrated that a LEM-like microcalorimeter will be able to detect the CGM of MW-mass galaxies to large radii $\sim R_{500}$, even in low-mass galaxies below the "transition" regime (Figure 1). Long exposure times with CCD instruments such as Chandra ACIS or XMM-Newton EPIC spent on individual massive galaxies have revealed only the innermost part of the CGM and at best give us a vague idea of the temperature structure, especially if they are not in an ongoing starburst phase. Bogdán et al. (2013a) used Chandra to image NGC 266, a massive ($M_{200} \approx 8 \times 10^{12} M_\odot$) nearby galaxy, and detected the CGM out to about 60 kpc, which is about 20% of R_{500}. Bogdán et al. (2017) used XMM-Newton to detect and characterize the CGM around the massive galaxy NGC 6753, which has a virial mass of $10^{13} M_\odot$. The authors could reliably make a detection out to 50 kpc, before background systematics made any conclusions impossible. This is about 17% of R_{500}. These exceptional cases demonstrate that only with massive efforts are we currently able to explore up to 1% of the volume that the CGM fills out to R_{500}, and this is only for the most massive, hand-picked galaxies, which are at the high-mass end. Our mock observations show that with a large-grasp microcalorimeter we can not only detect these types of galaxies beyond R_{500} (see the green profiles in Figures 6 and 7) in individual lines, such as O VIII, but also map their dynamical, thermal, and chemical abundances. These galaxies are expected to be dominated by AGN feedback, which we see as outbursts on the velocity map or the O/Fe ratio map. Features of the abundance ratio map such as high O/Fe ratios may be indicative of strong early feedback or a recent starburst, whereas a high abundance of metals from AGB winds, such as carbon and nitrogen, may be evidence for efficient gas entrainment from the ISM in SN-driven winds (e.g., Nomoto et al. 2006; Das et al. 2019b; Carr et al. 2023).

A LEM-like instrument will explore unknown territory by also mapping galaxies of much lower mass, down to $M_{200} \approx 3 \times 10^{11} M_\odot$, which has not been done so far. For these lowest-mass galaxies, depending on the SFR, radial profiles can be derived out $0.5 R_{500}$. In this regime, we do not

expect AGNs to be important in the feedback cycle, while stellar winds are expected to enrich and reheat the CGM.

The details of the transition from stellar to AGN feedback are largely not understood and are implemented ad hoc in simulations to match some observational constraints, such as stellar scaling relations ($M - \sigma$, $M_\star - M_{halo}$, galaxy morphologies, quiescent fractions as a function of stellar mass, and $SFR-z$ relations). Many measurements by a LEM-like observatory can be conducted that will lead to a new understanding of the processes within the CGM, such as central regions, where a spectral continuum of the CGM emission can be measured, allowing us to constrain the absolute metal abundance, and at larger radii, the steepening of the X-ray line emission to distinguish the contribution from SN feedback, as seen, e.g., between EAGLE and TNG100, where TNG100 produces centrally peaked profiles with a steeper decrease in surface brightness (see, e.g., Chadayammuri et al. 2022 for a comparison of profiles with simulations that have different feedback mechanisms). Measurements of the X-ray luminosities, surface brightness profiles, and temperature distributions that relate to the outflow energies will show if the gas is ejected from the the disk and allow one to distinguish if feedback is instantaneously stopping a cooling flow or whether a cumulative feedback effect is preventing gas phases from cooling (Davies et al. 2019b; Oppenheimer et al. 2020; Terrazas et al. 2020; Truong et al. 2020). With a few assumptions, such as a metallicity profile, a total gas mass can be derived. Supplementary SZ (e.g., Wu et al. 2020; Bregman et al. 2022; Moser et al. 2022) or fast radio burst observations (e.g., Ravi 2019; Macquart et al. 2020; Wu & McQuinn 2023) will also help to derive the gas mass. The impact of the central AGN will be observed in the range of azimuthal asymmetry observed in the CGM emission.

Chadayammuri et al. (2022) and Comparat et al. (2022) have demonstrated, through the stacking of optically detected galaxies in the eROSITA Final Equatorial Depth Survey, that the X-ray-bright CGM exists even in low-mass galaxies. Based on these results, simulations such as EAGLE and TNG100 are likely underestimating the surface brightness, especially in the low-mass regime (see, e.g., the $2.5 \times 10^{10}\,M_\odot$ stellar mass bin in Figure 4 of Chadayammuri et al. 2022, which is a factor of 3–5 above the simulation predictions). Furthermore, the dichotomy between star-forming galaxies being brighter in simulations with respect to quiescent galaxies might not be true, at least not to the extent that it is predicted. Quiescent galaxies with little to no star formation tend to have massive and dominant AGNs and are well suited to understanding the AGN cycles. These results cast doubt on the validity of the Simba CGM profiles, as Simba appears to drive gas to too large radii, making the galaxy halos fainter than observed by Chadayammuri et al. (2022). Simba also appears to be too X-ray-faint, compared to low-mass groups (Robson & Davé 2020), as the energy output from the bipolar jets evacuates the halos. Although stacking analyses have provided some distinctions among the simulations, stacking cannot replace detailed analyses of individual galaxies, as it might be biased by a few bright objects.

4.3. Observing Strategies

In the previous sections, we demonstrated that a LEM-like mission with a large-grasp microcalorimeter will be able to map nearby galaxies over a wide range of masses, SFRs, and black
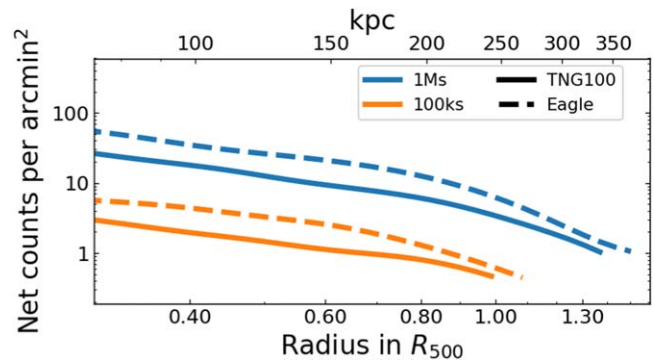

Figure 13. Median O VIII surface brightness profile of the total high-mass samples of EAGLE (dashed lines) and TNG100 (solid lines) for two simulated exposure times, 1 Ms (blue), and 100 ks (orange) for a mission such as the LEM. Each profile ends where the criteria for statistical and systematic uncertainties are not fulfilled (see Section 2.3.3).

hole masses. We argued that an instrument such as the Athena X-IFU will not be able to dedicate enough observing time to this science area. However, even an observatory such as LEM will not be able to spend 1 Ms on 120 galaxies that we assume to have observations available (40 in each of the three mass samples). We tested the impact on constraining the line surface brightness distribution with shorter observations (Figure 13), and found that even with 100 ks per galaxy, a LEM-like mission will be able to map the O VIII emission out to R_{500}, in both EAGLE and TNG100 simulated galaxies. In an observing plan for a LEM-like mission, fainter galaxies will take up significantly more observing time, especially in the crucial transition regime of MW-mass galaxies. Having 10 low-, 10 medium-, and 10 high-mass galaxies, where each galaxy is observed for 1 Ms, with the exception of the high-mass halos (100 ks), one can achieve such an ambitious program within about 20 Ms, which is a typical directed science program for a probe-class mission. While the trend of the average properties (e.g., O VIII brightness) in each mass bin is important, the dispersion around the median also will be important to understand. Therefore, galaxies should be selected to cover a range of properties that might shape the CGM, such as the stellar mass $M_\star$ at a given halo mass, the SFR, and the mass of the SMBH.

We also tested whether dedicated background observations are necessary or whether surface brightness profiles can be extracted using a model of the foreground and background emission. This model can be fit to the same observation in an outer region and then constrain the expected background plus foreground counts in each annulus at the CGM line spectral window. This method achieves comparable results, and reduces the overhead, but requires a good model of the foreground spectrum.

5. Summary

Mapping the X-ray emission of the hot CGM is one important key to understanding the evolution of galaxies from smaller galaxies with star-formation-driven feedback to larger, quiescent galaxies. MW-mass galaxies appear to be at the transition point between these regimes. However, the current generation of X-ray instruments is unable to capture the emission from the hot CGM that is dominant in the soft X-ray band and distinguish it from the bright MW foreground. We demonstrate that a high-spectral-resolution microcalorimeter

with a large FoV and large effective area can not only detect the CGM line emission to R_{500}, but also can map the individual physical properties, such as temperature and velocity. A mission designed to study the hot CGM, similar to LEM probe concept, will transform all fields of astrophysics (Kraft et al. 2022).

We created realistic mock observations, based on hydrodynamical simulations from EAGLE, IllustrisTNG, and Simba, for a large-effective-area instrument with 2 eV spectral resolution and a $32' \times 32'$ FoV. We included all background and foreground components in these mock observations. The galaxies span a mass range from $\log M_{200}[M_\odot] = 11.5 - 13$ and have been divided into three samples, based on their halo mass, to represent the dominating feedback regime. For the mock observations, the low- and medium-mass galaxies (up to $\log M_{200}[M_\odot] \leqslant 12.5$) are placed at $z = 0.01$, while the high-mass galaxies are at $z = 0.035$ and an exposure time of 1 Ms is used. For each galaxy, we constrain the surface brightness profile of the O VII(f), O VIII, Fe XVII (725 and 729 eV), and C VI lines. For galaxies at $z = 0.035$, we also include the O VII (r) and the Fe XVII (826 eV) lines, but have to omit the Fe XVII (729 eV) line, since it is blended with the MW foreground. Our findings are summarized as follows:

1. The median galaxy surface brightness profile for MW-sized galaxies at $z = 0.01$ can be traced to R_{500}, which is typically 170 kpc or $14'$.
2. The CGM in more massive galaxy halos up to $\log M_{200} = 13$ at $z = 0.035$ can be measured out to R_{200}. Even for the lowest-mass halos (down to $\log M_{200} = 11.5$), we typically will measure CGM emission to $\sim 0.5 R_{500}$.
3. The O VIII emission line is brightest in most cases, followed by O VII and Fe XVII.
4. Subdividing the galaxy samples by SFR reveals that star-forming TNG100 galaxies are brighter in the core.
5. There is significant scatter in the CGM brightness due to galaxy-to-galaxy variation. Also, the different simulations produce slightly different CGM luminosities at a given mass scale, where EAGLE galaxies are brightest, especially at higher masses, and Simba galaxies are typically the faintest, due to the strong AGN feedback expelling the gas.
6. We demonstrate that the O VII-to-O VIII line ratio in the mock observations can be used as a temperature tracer out to R_{500} for more massive galaxies at $z = 0.035$ and to $0.5 R_{500}$ for the less massive galaxies at $z = 0.01$. We find that EAGLE galaxies are hotter in the center compared to TNG100, while having similar line ratios to TNG100 at large radii.
7. We are able to map the substructure of galaxies out to R_{500} by quantifying the azimuthal asymmetry. Interestingly, we find that TNG100 and Simba galaxies with a smaller SMBH reach high values of substructure beyond $0.4 R_{500}$, while EAGLE galaxies do not show that level of clumping. For massive SMBHs, all simulations predict lower CGM clumping factors. This observable appears to be crucial to understanding the mechanisms of AGN feedback, as it directly points to the efficiency of the AGN in pressurizing the CGM gas.
8. Finally, we test the 2D properties of the gaseous halos around galaxies with spectral maps of properties, such as the temperature, the LOS velocity, and the O/Fe ratio. Together, these quantities can be used to pinpoint

signatures of AGN feedback, such as the AGN duty cycle or energy output.

A LEM-like mission would revolutionize our understanding of the CGM, placing dramatic new constraints on the variety of numerical simulations and on key feedback processes.

Appendix A
Analysis Details

The analysis of simulated microcalorimeter observations of nearby galaxies resembles the traditional X-ray analysis. However, a few details have been altered to take advantage of the high spectral resolution. We describe these here in more detail.

A.1. Point-source Removal

The point sources in the simulated event files are detected through `wavdetect` in the (1–1.4) keV band, where only the CXB and non-X-ray background (NXB) dominate. At softer energies, the Galactic emission will dominate, and at higher energies, the particle background will dilute the CXB signal due to the decrease in effective area. We show in Figure 14 (left) the distribution of cumulative number counts as a function of the threshold flux S (in net source counts within a 1 Ms observation). The distribution is consistent with the expected trend based on the Chandra observations by Lehmer et al. (2012), where a broken power law is found for distant AGNs and galaxies. If we excise the 50 brightest sources (Figure 14, right), we remove about 50% of the total flux in point sources, while only removing about 2% of the detector area. For the 100 brightest sources, we would remove more than 4% of the area and 60% of the flux, and if we removed 250 sources, we would excise 75% of the flux and almost 10% of the total detector area.
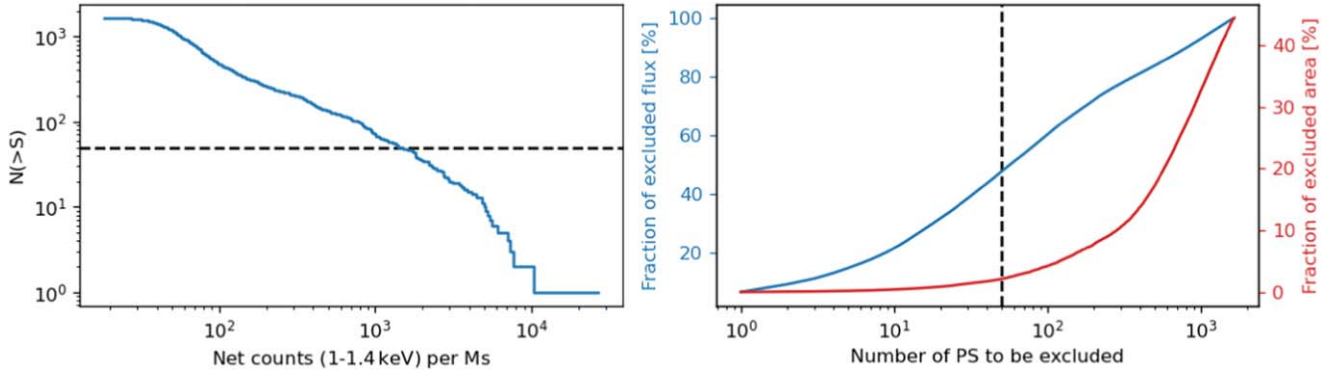
Figure 14. Removal of point sources in the observation. Left: cumulative number counts as a function of flux (in net counts). Right: the blue line represents the fraction of excised flux in point sources as a function of the number of point sources (highest-flux sources first), and the red line shows, for the same number of excised point sources, the area fraction that is masked.

A.2. Surface Brightness Extraction

In order to trace the emission lines (such as O VIII) in a narrow band out to large radii, it is important to quantify the background precisely. While the MW foreground should be greatly reduced, due to the redshift, the exact level of the background is still crucial, when we want to make a detection with a signal that is only 10% of the total background level. We separate the background components into the MW foreground (LHB, GHE, and NPS), the unresolved/unremoved point-source contribution from distant AGNs and galaxies (CXB), and the interaction of charged particles (galactic cosmic rays) with the detector and/or the satellite (producing secondary particles, such as fluorescent X-rays or electrons), which is not focused by the mirrors (NXB). The modeling of these components in our simulated X-ray observations has been described in Section 2.2.

To estimate the background counts in a narrow band at the redshifted CGM line, we take a blank-field observation without a science target and spatially close to the observation of each nearby galaxy of interest. We assume that the MW foreground emission does not vary within the FoV of our observation and is also consistent with the MW foreground in the blank-field observation. The same assumption is made for the NXB, although its contribution is less important at the emission lines of interest. Our focus is set on the CXB contribution to the total background, as it is different not only between the blank field and the galaxy observation, but also varies slightly from each extraction region (annulus) of the surface brightness profile. Therefore, we include a CXB correction factor to the blank-field background counts that is determined from the hard band (e.g., (1–1.4) keV), where the MW component is insignificant.

We label the extracted total counts (CGM and total background) in a narrow line band and small extraction region within our observation as cts_{line}^{Obs}. We define the counts in the broad band and the blank-field observation (Bkg) accordingly:

$$cts_{line}^{Obs} = CGM_{line}^{Obs} + MW_{line}^{Obs} \\ + CXB_{line}^{Obs} + NXB_{line}^{Obs} = CGM_{line}^{Obs} + \mathcal{B}_{line}^{Obs}, \quad (A1)$$

$$cts_{broad}^{Obs} = CGM_{broad}^{Obs} + MW_{broad}^{Obs} + CXB_{broad}^{Obs} \\ + NXB_{broad}^{Obs} = CGM_{broad}^{Obs} + \mathcal{B}_{broad}^{Obs}, \quad (A2)$$

$$cts_{line}^{Bkg} = MW_{line}^{Bkg} + CXB_{line}^{Bkg} + NXB_{line}^{Bkg} = \mathcal{B}_{line}^{Bkg}, \quad (A3)$$

$$cts_{broad}^{Bkg} = MW_{broad}^{Bkg} + CXB_{broad}^{Bkg} + NXB_{broad}^{Bkg} = \mathcal{B}_{broad}^{Bkg}. \quad (A4)$$

Note that the MW and NXB components scale between the observation and blank-field region only with the area (the observing time has already been taken into account), and in the broad band, the CGM component has no real contribution. We utilize a broad band above 1 keV (e.g., (1–1.4) keV; see Figure 15) to estimate the difference in the CXB between our extraction region in the observation and the total blank field (the whole FoV).

We derive a scaling factor,

$$f_{broad} = \frac{cts_{broad}^{Obs}}{f_A \times \mathcal{B}_{broad}^{Bkg}}, \quad (A5)$$

where f_A is the ratio of the extraction area of the observation and the background. f_{broad} is typically close to 1, especially if the extraction region in the observation is large (outer annuli). In order to minimize Poisson noise, we estimate the narrow-line-band background from the entire blank-field observation and scale it by the area and f_{broad}. We tested this method with a randomly chosen galaxy halo from TNG100 (ID 419061) and defined seven radial bins of $0.15R_{500}$ width to reach an outer radius of $1.05R_{500}$. In each of these regions, we extracted the spectrum from the observation and fitted it with the model components (see, e.g., Figure 15), so we have a precise knowledge of the background components and the CGM emission. From the fitted model components, we are able to calculate the precise total background in each annulus $\mathcal{B}_{line}^{Obs}$, as well as the CGM counts CGM_{line}^{Obs}, and make a comparison with the corrected blank-field background estimate, $\mathcal{B}_{line}^{Bkg} \times f_{broad}$. We find that the difference in counts between the actual background, $\mathcal{B}_{line}^{Obs}$, and the blank-field-predicted background is always much less than 1% of the CGM counts in each annulus (reaching 0.5% around R_{500}). Therefore, we employ this method of scaling the blank field by the broadband CXB contribution to estimate the background. Deriving the background from the spectral fit is computationally expensive and not feasible for each galaxy and extraction region.

In order to define statistically significant radial bins of the surface brightness profile, we require a minimum S/N of 3. The signal is directly calculated from the measured cts_{line}^{Obs} minus the background estimate $\mathcal{B}_{line}^{Bkg} \times f_{broad}$. The noise is
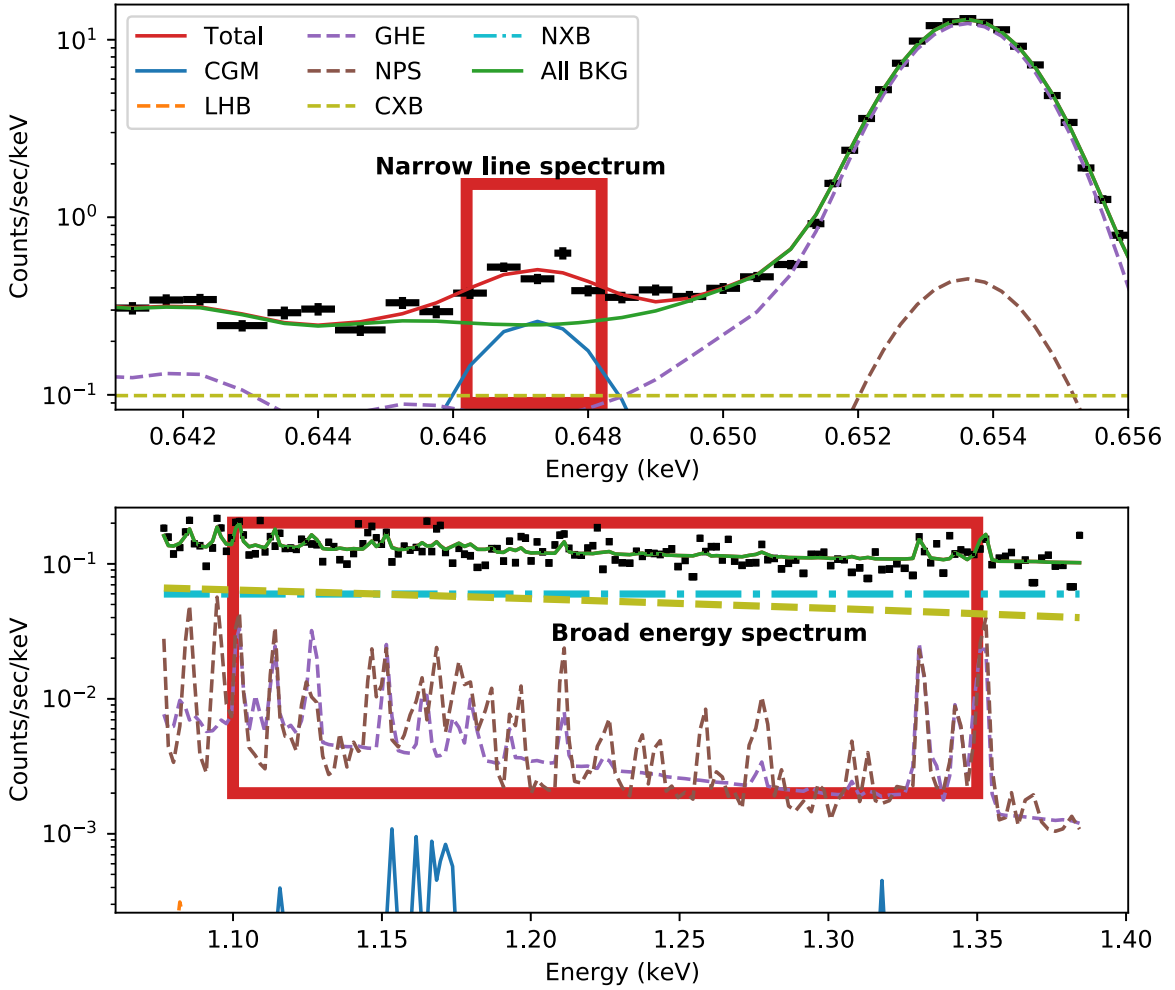
Figure 15. Narrow and broad bands for estimating the CXB scaling of the total background.

assumed to be

$$
\text{Noise} = \sqrt{\text{cts}_{\text{line}}^{\text{Obs}} + \mathcal{B}_{\text{line}}^{\text{Obs}} \times (1 - f_{\text{broad}}) + 0.1 \times \mathcal{B}_{\text{line}}^{\text{Obs}}} ,
$$

(A6)

where we account for systematic uncertainties in the background as well as uncertainties in the CXB contribution.

We also tested the impact of MW foreground uncertainties on the narrow-line counts. With the typical uncertainties of the foreground model fitting (using only the narrow lines of C VI, O VII, O VIII, and Fe XVII) in the temperature, e.g., of the LHB, we find a difference in background counts of less than 1% of the CGM counts.

Appendix B
Deviation from CIE

In low-density plasmas, the photoexcitation and ionization rates can become high relative to the electron collisional excitation and ionization rates, which affects emission lines. Therefore, the ratio of emission lines (e.g., O VII and O VIII) is no longer independent of the gas density, as in CIE (Churazov et al. 2001; Khabibullin & Churazov 2019). To estimate the effect for typical galaxy halos, we simulate the hot-gas distribution with a simple β-model ($\beta = 0.4$, $r_c = 40$ kpc; see

Li et al. 2017; Zhang et al. 2024). The hot CGM mass is assumed to be the baryonic mass (7.5% halo mass) minus stellar mass (4% halo mass). For a given halo mass, we can estimate the density at a given radius, and we assume the temperature to be close to the virial temperature (Ponti et al. 2023):

$$
k_{\text{B}} T_{\text{vir}} = \frac{2}{3} G \mu m_{\text{p}} \frac{M_{\text{vir}}}{r_{\text{vir}}} ,
$$

(B1)

where $\mu = 1.32$ is the mean molecular weight of the gas (Ponti et al. 2023), G is the gravitational constant, and m_{p} is the proton mass. We derive the line ratios of both O VII(f) to O VIII and the coadded O VII(f+r) to O VIII, and we quantify the difference to the simple case of CIE. The results are shown in Figure 16 (left): at a radial distance of R_{500} (the blue line), we see that for halos with a mass above $10^{12} M_{\odot}$, density-dependent effects are less than 8%. Closer to the center (the orange and green lines), the densities are higher and differences to CIE even smaller. At higher masses, above two times the MW ($\log M/M_{\odot} = 12.4$), the differences are negligible, even at R_{500}. We also find that the difference between the resonant and forbidden lines becomes less than 1% for higher-temperature (mass) halos, above densities of 10^{-4} cm^{-3} (Figure 16 right).
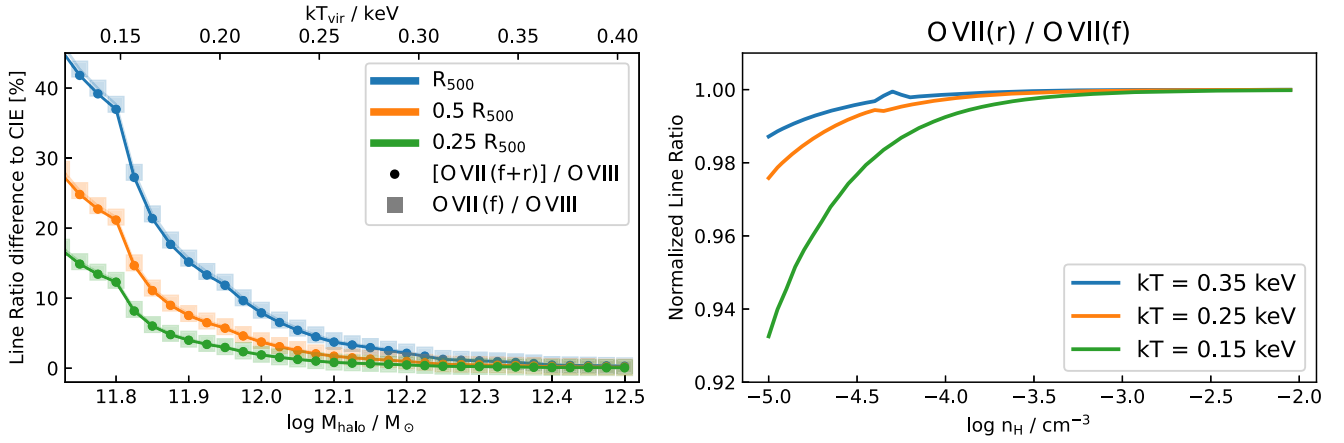
Figure 16. Left panel: difference in line ratio of O VII to O VIII with respect to the CIE line ratio for a set of halo masses. The dependence on the galaxy halo mass and the measurement of the line ratios are performed at specific radii (blue—R_{500}; orange—$0.5R_{500}$; and green—$0.25R_{500}$), assuming that the density profile follows a simple β-model and that the temperature is assumed to be the virial temperature. The black circles indicate the O VII line flux from the sum of the forbidden and resonant lines, while the gray circles use only the forbidden lines as the O VII flux. Right panel: CIE-normalized line ratios of the resonant to forbidden line of O VII for a given density, illustrating the fractional difference between between CIE and photoionized plasma that includes CXB resonant scattering. The three colors represent different temperatures.

Appendix C
List of Simulated Galaxy Halos

Tables 4, 5, and 6 list all the simulated galaxy halos that are used for the line surface brightness profiles, the line ratios, and the azimuthal substructure test. The columns denote the Halo ID/subID, the halo stellar mass within 30 kpc, the total halo mass M_{200}, the central black hole mass, the SFR, and R_{500}. As described in Section 2.2, we use three simulation suites—IllustrisTNG, EAGLE (100 Mpc box), and Simba (100 Mpc box)—and subselect from each 120 galaxies. These galaxies are equally divided into a low-mass sample $\log_{10} M_{200}/M_\odot = 11.5$–12, a medium-mass sample $\log_{10} M_{200}/M_\odot = 12$–12.5, and a high-mass sample $\log_{10} M_{200}/M_\odot = 12.5$–13. In Figures 17, 18, and 19, we show stacked O VII and O VIII images for each of the galaxies, including instrumental background, foreground emission, and CXB (see Section 2).

Table 4
Basic Properties of the Selected IllustrisTNG Halos

Halo	$M_\star$ ($10^{10}M_\odot$)	M_{200} ($10^{12}M_\odot$)	M_{BH} ($10^8M_\odot$)	SFR ($M_\odot$ yr^{-1})	R_{500} (kpc)	Halo	$M_\star$ ($10^{10}M_\odot$)	M_{200} ($10^{12}M_\odot$)	M_{BH} ($10^8M_\odot$)	SFR ($M_\odot$ yr^{-1})	R_{500} (kpc)
TNG100 Low-mass Sample											
582879	0.63	0.33	0.32	0.487	99	541402	1.27	0.64	0.54	1.189	123
539812	1.56	0.63	0.62	0.418	125	581475	1.71	0.34	0.86	0.076	102
513718	3.71	0.95	1.25	2.564	142	530171	0.98	0.75	0.22	1.217	125
509402	3.21	0.96	1.08	0.507	142	489863	1.99	0.99	0.79	4.143	130
505030	2.49	0.84	0.54	2.334	138	513262	3.98	0.97	1.89	0.000	142
557923	1.31	0.49	0.34	1.372	114	512631	0.44	0.93	0.19	0.667	143
562983	0.29	0.38	0.09	0.466	94	509468	4.90	0.96	1.01	4.559	144
551694	1.04	0.49	0.41	0.967	111	567124	1.01	0.47	0.57	1.141	113
537893	1.24	0.44	0.53	1.357	110	525081	1.77	0.84	0.88	6.793	135
524295	2.99	0.82	0.98	2.155	135	539998	2.16	0.66	1.01	0.534	127
562544	0.52	0.51	0.23	0.479	116	528531	1.43	0.86	0.81	1.569	141
555033	0.77	0.37	0.36	0.623	103	554843	0.41	0.50	0.13	0.402	109
556431	2.02	0.61	1.35	0.000	122	505616	4.03	0.98	1.66	0.000	145
538080	3.26	0.70	1.35	0.000	129	523231	2.35	0.81	0.78	1.281	135
559158	1.43	0.45	0.50	1.081	106	558021	1.10	0.52	0.32	1.231	116
520230	1.68	0.73	0.53	0.885	130	465921	0.91	0.78	0.39	1.842	127
506526	2.07	0.89	1.17	1.163	134	505680	0.34	0.38	0.08	0.403	87
578707	0.43	0.34	0.30	0.449	99	567178	1.42	0.44	0.29	1.512	112
589067	1.00	0.35	0.59	0.306	103	567085	0.63	0.41	0.22	0.970	107
547892	1.76	0.58	1.06	1.285	121	549236	0.67	0.50	0.31	0.774	110
TNG100 Medium-mass Halos											
497646	4.90	1.09	0.91	2.781	149	497800	4.45	1.20	1.56	0.000	156
487244	6.27	1.20	1.56	2.622	155	490577	6.15	1.30	1.50	0.005	160
421835	7.19	3.10	1.69	0.177	208	419061	3.76	1.92	1.01	5.303	164
460273	6.27	1.79	2.39	0.005	175	484427	5.20	1.38	1.90	0.000	157
422831	6.59	2.97	2.70	0.000	203	449034	8.66	2.34	2.75	0.000	189
411321	6.72	1.93	1.80	0.479	172	449549	7.59	2.24	2.28	0.000	189
428813	6.57	2.70	1.75	0.002	199	442855	7.61	2.24	2.47	0.001	188

Table 4
(Continued)

Halo	$M_\star$ $(10^{10}M_\odot)$	M_{200} $(10^{12}M_\odot)$	M_{BH} $(10^8M_\odot)$	SFR $(M_\odot\,yr^{-1})$	R_{500} (kpc)	Halo	$M_\star$ $(10^{10}M_\odot)$	M_{200} $(10^{12}M_\odot)$	M_{BH} $(10^8M_\odot)$	SFR $(M_\odot\,yr^{-1})$	R_{500} (kpc)
483900	5.75	1.31	1.61	0.718	159	460746	8.07	1.86	2.49	0.015	174
444545	5.25	2.79	3.56	0.000	200	438996	5.76	1.78	2.60	0.000	172
463453	5.26	1.59	1.89	0.000	163	494771	4.13	1.11	1.04	3.695	149
461136	6.04	1.80	1.81	0.117	177	493920	5.39	1.40	2.56	0.000	162
432711	8.37	2.67	2.62	0.649	198	471801	4.27	1.32	1.83	0.000	155
418230	8.11	2.42	1.61	0.019	192	428158	7.14	2.95	3.57	0.000	207
417281	5.60	2.39	1.55	5.086	185	433537	4.76	2.65	3.24	0.000	196
459270	4.32	2.14	2.95	0.000	187	426764	8.91	2.39	2.65	0.248	187
462391	4.59	1.90	2.11	0.000	175	460823	5.29	1.98	2.19	0.000	179
436233	5.18	2.63	2.75	0.000	196	456014	4.82	2.04	1.70	0.000	173
432831	5.17	2.97	3.41	0.000	206	480587	5.02	1.43	2.23	0.000	161
426483	10.13	2.88	3.15	0.002	205	471109	6.03	1.50	1.47	0.021	164
458378	6.63	2.19	2.72	0.000	184	469930	7.65	1.51	1.58	1.236	166
TNG100 High-mass Halos											
390859	8.48	4.75	4.49	0.000	237	415373	9.43	3.66	4.95	0.000	219
383307	10.31	4.87	4.52	0.365	232	332068	8.15	5.34	2.78	0.034	217
387236	12.15	4.46	3.65	0.865	230	341356	11.92	7.18	5.27	0.064	273
377398	17.08	6.09	5.98	0.003	260	414447	8.42	3.44	3.35	0.000	211
333672	10.32	8.70	2.34	0.472	288	312412	13.09	7.79	4.97	0.000	282
394439	12.03	4.29	3.39	1.286	230	399520	8.74	3.93	4.83	0.000	220
249164	13.77	9.95	6.87	0.069	298	372568	13.64	5.53	5.60	0.104	254
413091	12.81	3.67	2.39	0.021	218	342689	13.01	4.74	3.69	0.201	238
346420	11.97	5.31	5.37	0.056	244	359639	14.99	6.41	7.83	0.456	261
360916	5.75	5.98	4.77	0.000	238	405460	12.18	3.23	5.59	0.000	206
345812	10.51	8.82	3.41	5.729	295	288014	7.10	9.55	2.24	0.246	292
384103	6.69	4.91	2.94	0.010	218	339547	11.91	7.57	4.71	0.000	271
359086	8.14	7.75	4.70	0.000	283	382059	11.56	3.80	2.87	2.505	221
377212	14.52	5.98	7.86	0.079	258	376132	7.35	3.61	4.06	0.000	214
337444	10.97	7.94	6.50	0.000	278	329105	14.29	8.71	8.22	1.058	294
361418	6.22	6.46	4.64	0.000	252	399969	11.73	4.23	4.43	0.000	227
313402	10.00	9.02	6.59	0.002	245	386429	9.24	4.78	1.69	4.350	208
327822	10.97	4.27	2.22	4.068	222	371859	8.90	5.62	7.07	0.000	253
298206	12.79	8.75	5.82	1.032	282	398110	11.38	4.01	4.98	0.033	230
312891	15.21	9.78	11.30	0.088	303	380119	12.16	4.85	5.02	0.290	239
TNG50 Halos											
358608	15.06	5.04	4.38	4.018	243	467415	8.68	2.08	2.13	9.224	183

Table 5
Basic Properties of the Selected EAGLE Halos

Halo	$M_\star$ $(10^{10}M_\odot)$	M_{200} $(10^{12}M_\odot)$	M_{BH} $(10^8M_\odot)$	SFR $(M_\odot\,yr^{-1})$	R_{500} (kpc)	Halo	$M_\star$ $(10^{10}M_\odot)$	M_{200} $(10^{12}M_\odot)$	M_{BH} $(10^8M_\odot)$	SFR $(M_\odot\,yr^{-1})$	R_{500} (kpc)
Low-mass Sample											
2703	0.45	0.42	0.02	0.691	104	2144	0.79	0.44	0.01	0.292	110
2258	0.27	0.52	0.02	0.477	109	2824	0.66	0.44	0.01	0.431	109
2577	0.21	0.37	0.00	0.498	95	1949	1.15	0.69	0.02	1.131	125
2578	1.15	0.52	0.01	0.480	117	1791	0.99	0.86	0.05	0.606	139
2044	1.07	0.71	0.01	0.190	117	2478	0.53	0.39	0.02	0.306	104
2535	0.71	0.51	0.02	0.614	114	2370	0.92	0.55	0.02	0.992	117
1662	1.32	0.85	0.07	1.099	133	2428	0.41	0.33	0.01	0.411	98
2899	0.40	0.38	0.01	0.750	98	2726	0.71	0.53	0.08	0.000	119
2592	1.14	0.50	0.05	0.205	115	1730	2.86	0.78	0.05	1.402	132
2345	0.36	0.53	0.01	0.230	117	2864	0.56	0.41	0.01	0.355	105
2557	0.28	0.37	0.02	0.326	98	2516	0.83	0.48	0.03	0.434	113
2671	0.25	0.48	0.01	0.408	100	1725	1.93	0.81	0.11	0.003	131
2118	0.85	0.39	0.01	0.823	105	2902	0.36	0.38	0.01	0.241	97
1647	2.13	0.87	0.08	0.577	138	2874	0.31	0.39	0.02	0.147	105
2184	1.47	0.65	0.03	0.690	125	1803	1.64	0.73	0.03	1.379	128

Table 5
(Continued)

Halo	$M_\star$ (10^{10}M$_\odot$)	M_{200} (10^{12}M$_\odot$)	M_{BH} (10^{8}M$_\odot$)	SFR ($M_\odot$ yr^{-1})	R_{500} (kpc)	Halo	$M_\star$ (10^{10}M$_\odot$)	M_{200} (10^{12}M$_\odot$)	M_{BH} (10^{8}M$_\odot$)	SFR ($M_\odot$ yr^{-1})	R_{500} (kpc)
1581	1.21	0.82	0.12	0.018	123	2688	0.73	0.52	0.04	0.338	115
2176	1.09	0.68	0.01	0.547	124	2338	0.29	0.63	0.03	0.304	125
1564	2.37	0.92	0.07	0.885	140	2852	0.63	0.46	0.04	0.578	112
2716	0.56	0.42	0.01	0.478	100	1569	1.50	0.84	0.03	0.983	132
2066	1.59	0.69	0.05	0.768	126	2157	1.43	0.59	0.05	1.220	121
Medium-mass Halos											
1096	2.81	1.45	0.28	0.111	160	798	4.79	1.67	0.31	0.010	162
700	4.45	2.70	0.81	1.100	201	816	4.28	1.86	0.07	2.487	170
521	2.76	2.19	0.73	0.255	185	1256	1.61	1.20	0.04	0.776	155
480	6.90	3.12	0.76	0.218	203	1303	1.44	1.27	0.06	0.632	156
964	4.46	1.55	0.04	2.218	166	846	2.02	1.82	0.23	0.041	164
789	2.47	2.19	0.47	0.000	189	1233	2.02	1.06	0.10	0.548	144
1244	2.56	1.10	0.27	1.034	147	774	4.40	2.20	0.53	0.021	185
965	2.84	1.53	0.28	0.577	158	1133	3.28	1.28	0.16	1.896	153
1350	2.59	1.05	0.15	1.869	147	1296	3.15	1.09	0.26	0.910	149
927	5.02	1.83	0.49	1.128	179	833	5.81	2.03	0.79	2.467	182
482	4.98	2.67	0.58	1.394	198	660	5.16	2.23	0.14	7.143	183
744	3.43	2.06	0.72	0.053	183	1122	3.16	1.51	0.31	0.500	165
1205	2.47	1.06	0.19	1.044	144	597	4.57	3.01	0.48	2.220	203
933	3.30	1.74	0.52	0.000	170	977	3.68	1.63	0.30	1.095	168
527	4.90	2.92	0.80	2.603	196	914	2.22	1.53	0.02	3.448	164
1142	2.33	1.25	0.49	0.024	155	961	1.82	1.69	0.39	0.000	168
1117	3.30	1.32	0.13	2.053	155	835	3.91	1.79	0.08	2.951	173
512	4.32	2.70	0.39	2.959	196	622	3.81	3.03	0.41	1.113	207
621	4.63	2.41	0.10	2.462	177	689	2.65	2.14	0.27	0.412	175
709	3.29	2.35	0.24	1.544	178	577	4.82	2.42	0.45	1.189	181
High-mass Halos											
207	8.57	4.86	0.34	6.738	223	218	6.27	7.19	1.27	0.533	261
214	12.05	8.57	2.52	0.101	294	262	8.67	6.05	1.67	0.094	255
209	9.18	8.53	2.77	2.621	287	541	8.47	3.29	1.22	1.588	210
235	7.45	6.75	1.71	3.997	264	399	5.15	3.89	2.18	0.000	226
251	9.04	6.17	2.02	3.160	252	342	4.51	3.89	1.20	0.199	224
253	9.42	6.85	1.34	4.110	262	132	11.83	6.70	1.35	1.723	255
244	8.89	6.58	0.89	4.195	255	169	7.16	9.12	0.68	4.680	256
377	9.35	4.19	0.85	0.538	222	224	5.07	4.59	1.44	2.278	236
283	6.32	5.87	1.17	3.746	252	231	13.12	7.43	2.13	0.000	271
208	8.55	3.93	1.21	0.000	226	422	6.10	4.14	0.91	1.463	230
282	3.92	5.62	0.27	2.259	219	141	12.53	8.53	2.14	4.794	285
189	12.05	7.94	4.10	0.124	275	121	9.44	9.98	2.75	1.904	298
248	4.91	5.62	2.34	0.081	247	439	6.53	3.58	0.66	3.127	212
151	13.37	9.33	2.03	4.601	285	203	9.59	4.32	1.53	1.344	229
194	11.61	8.99	1.71	3.159	277	360	8.57	4.95	1.52	0.008	240
539	6.25	3.24	1.01	0.019	210	177	8.83	9.25	2.88	2.211	292
427	6.19	4.05	0.79	0.765	223	254	11.07	7.55	1.64	0.385	274
334	8.81	5.09	1.80	0.000	240	243	7.60	7.78	0.21	0.124	277
408	6.70	4.39	0.30	3.627	227	277	3.39	4.65	0.43	1.054	212
276	8.18	4.37	1.13	0.104	221	337	8.00	5.22	1.60	0.793	235

Table 6
Basic Properties of the Selected Simba Halos

Halo	$M_\star$ (10^{10}M$_\odot$)	M_{200} (10^{12}M$_\odot$)	M_{BH} (10^{8}M$_\odot$)	SFR ($M_\odot$ yr^{-1})	R_{500} (kpc)	Halo	$M_\star$ (10^{10}M$_\odot$)	M_{200} (10^{12}M$_\odot$)	M_{BH} (10^{8}M$_\odot$)	SFR ($M_\odot$ yr^{-1})	R_{500} (kpc)
Low-mass Sample											
4721	1.94	0.93	0.51	1.702	140	6326	1.38	0.68	0.28	2.072	126
5266	0.63	0.75	0.04	1.432	128	4496	1.43	0.94	0.16	4.941	133
7185	1.60	0.58	0.24	1.664	121	6991	1.10	0.50	0.20	1.610	109
3729	1.68	0.97	0.43	2.214	124	5205	2.40	0.83	0.12	2.447	136
7837	0.91	0.49	0.17	2.523	113	4172	1.34	0.93	0.38	1.880	135
5566	1.74	0.60	0.49	1.522	119	11638	0.83	0.32	0.05	1.070	98

Table 6
(Continued)

Halo	$M_\star$ ($10^{10}M_\odot$)	M_{200} ($10^{12}M_\odot$)	M_{BH} ($10^8M_\odot$)	SFR ($M_\odot$ yr^{-1})	R_{500} (kpc)	Halo	$M_\star$ ($10^{10}M_\odot$)	M_{200} ($10^{12}M_\odot$)	M_{BH} ($10^8M_\odot$)	SFR ($M_\odot$ yr^{-1})	R_{500} (kpc)
6542	1.42	0.60	0.37	1.558	122	4862	1.65	0.53	0.38	1.122	119
6652	1.18	0.50	0.26	2.086	111	5494	2.18	0.65	0.57	1.301	123
7552	1.63	0.58	0.27	1.385	119	4267	0.92	0.92	0.34	2.029	132
9143	0.87	0.47	0.09	1.036	111	6156	0.87	0.58	0.04	5.991	116
7189	0.85	0.62	0.14	1.226	115	3768	1.89	0.64	0.46	3.384	119
5263	2.38	0.51	0.56	3.635	113	5762	1.15	0.36	0.33	2.065	104
8135	0.83	0.38	0.16	1.581	103	4965	0.30	0.40	0.29	2.137	107
4672	0.95	0.97	0.24	1.679	140	5557	1.31	0.75	0.28	1.001	130
6084	1.18	0.35	0.18	2.453	100	9136	1.11	0.43	0.22	1.063	107
11327	1.04	0.33	0.24	1.031	101	6800	1.06	0.54	0.14	1.076	116
5936	0.93	0.39	0.21	2.142	102	8881	0.82	0.50	0.08	1.207	116
4439	1.65	0.73	0.47	1.755	126	11362	0.69	0.35	0.10	1.166	100
10409	0.70	0.37	0.11	1.507	103	5802	1.31	0.38	0.37	1.842	104
4802	3.35	0.91	0.44	4.681	141	5565	1.33	0.70	0.21	1.498	124

Medium-mass Halos

Halo	$M_\star$	M_{200}	M_{BH}	SFR	R_{500}	Halo	$M_\star$	M_{200}	M_{BH}	SFR	R_{500}
2788	7.33	1.34	0.87	5.462	158	2992	5.23	1.06	0.40	15.196	148
2722	4.66	1.55	0.93	10.480	159	2401	4.21	1.12	1.10	1.439	151
1323	6.02	2.22	0.96	3.030	170	1792	3.99	1.38	0.21	11.855	147
3956	4.32	1.13	0.40	5.601	150	1864	11.30	2.48	1.17	3.974	195
1278	7.51	2.37	1.30	2.963	180	2496	2.55	1.49	0.23	9.434	156
2132	11.38	2.12	0.77	4.576	188	1650	2.30	1.84	1.38	1.849	170
2030	4.23	1.79	0.49	4.188	160	2166	2.76	1.08	0.42	5.268	146
395	8.61	3.13	3.03	3.697	206	1201	6.09	2.33	1.25	1.188	180
2828	4.97	1.57	1.19	5.388	167	2622	2.52	1.47	0.99	1.495	157
2058	6.82	2.03	0.99	5.198	183	1380	6.64	3.13	0.61	1.297	209
2131	3.20	1.92	0.88	1.257	172	2089	6.11	2.23	1.74	1.040	186
4086	4.22	1.15	0.15	6.362	152	3606	5.71	1.23	1.43	2.548	154
1403	3.92	2.24	0.90	3.556	176	1726	7.23	1.99	2.01	6.853	179
1985	7.44	2.13	0.67	1.127	183	2081	5.61	2.19	0.40	9.351	191
1482	6.83	2.86	1.91	3.100	197	1942	15.99	2.56	0.63	5.588	199
2204	3.86	1.59	0.48	1.382	164	2790	5.33	1.58	0.29	14.680	168
3101	6.34	1.45	0.36	9.689	163	3409	3.16	1.12	1.04	2.281	148
1762	2.39	1.57	0.79	4.764	154	3012	4.14	1.49	1.02	3.209	163
2831	3.98	1.45	0.16	13.514	152	2036	10.33	2.31	1.31	5.877	193
2066	1.14	1.65	0.24	3.519	144	3883	8.74	1.22	0.55	1.652	158

High-mass Halos

| Halo	$M_\star$	M_{200}	M_{BH}	SFR	R_{500}	Halo	$M_\star$	M_{200}	M_{BH}	SFR	R_{500}
793	11.00	5.82	1.25	5.868	236	483	7.07	7.41	2.06	1.367	241
414	11.41	9.12	9.96	7.806	296	928	5.38	3.69	1.77	2.034	201
343	17.38	9.31	8.13	1.533	292	406	17.12	9.79	4.20	6.775	300
704	15.05	6.15	2.46	1.044	259	859	19.38	3.63	2.00	8.954	209
550	5.75	6.84	2.71	2.130	256	729	11.17	4.49	3.22	2.392	236
589	8.08	5.37	4.71	1.272	234	499	9.01	8.77	2.22	2.046	280
1101	13.65	4.24	1.20	5.909	231	533	9.96	8.53	4.88	1.674	283
606	8.68	7.33	1.81	1.538	276	576	6.72	4.69	4.46	3.734	233
797	5.25	5.10	3.96	2.142	242	981	19.67	3.73	2.51	1.825	220
587	6.22	6.79	3.92	5.185	244	530	10.34	7.74	7.76	1.340	259
422	6.25	3.88	3.30	7.754	204	792	4.40	5.33	2.31	1.513	242
1162	9.05	3.98	1.35	1.839	214	1250	5.21	3.48	2.66	1.492	195
675	6.11	7.43	3.49	1.278	269	303	10.63	7.19	4.63	4.744	267
663	5.61	5.19	2.86	3.604	239	521	9.28	6.21	1.21	4.473	200
647	10.31	7.93	4.45	1.167	283	1369	3.15	3.58	1.66	9.063	217
1302	4.14	3.16	1.78	2.846	202	1375	4.02	3.56	0.83	4.062	219
1264	11.70	3.60	0.96	4.972	218	930	5.35	4.52	0.83	3.742	226
410	9.51	9.42	4.18	1.048	303	1067	5.37	3.26	2.46	2.147	201
948	4.69	4.21	3.68	3.268	229	396	13.91	7.52	5.18	1.300	263
472	7.78	7.03	3.55	2.297	257	1343	11.42	3.41	0.34	1.601	216
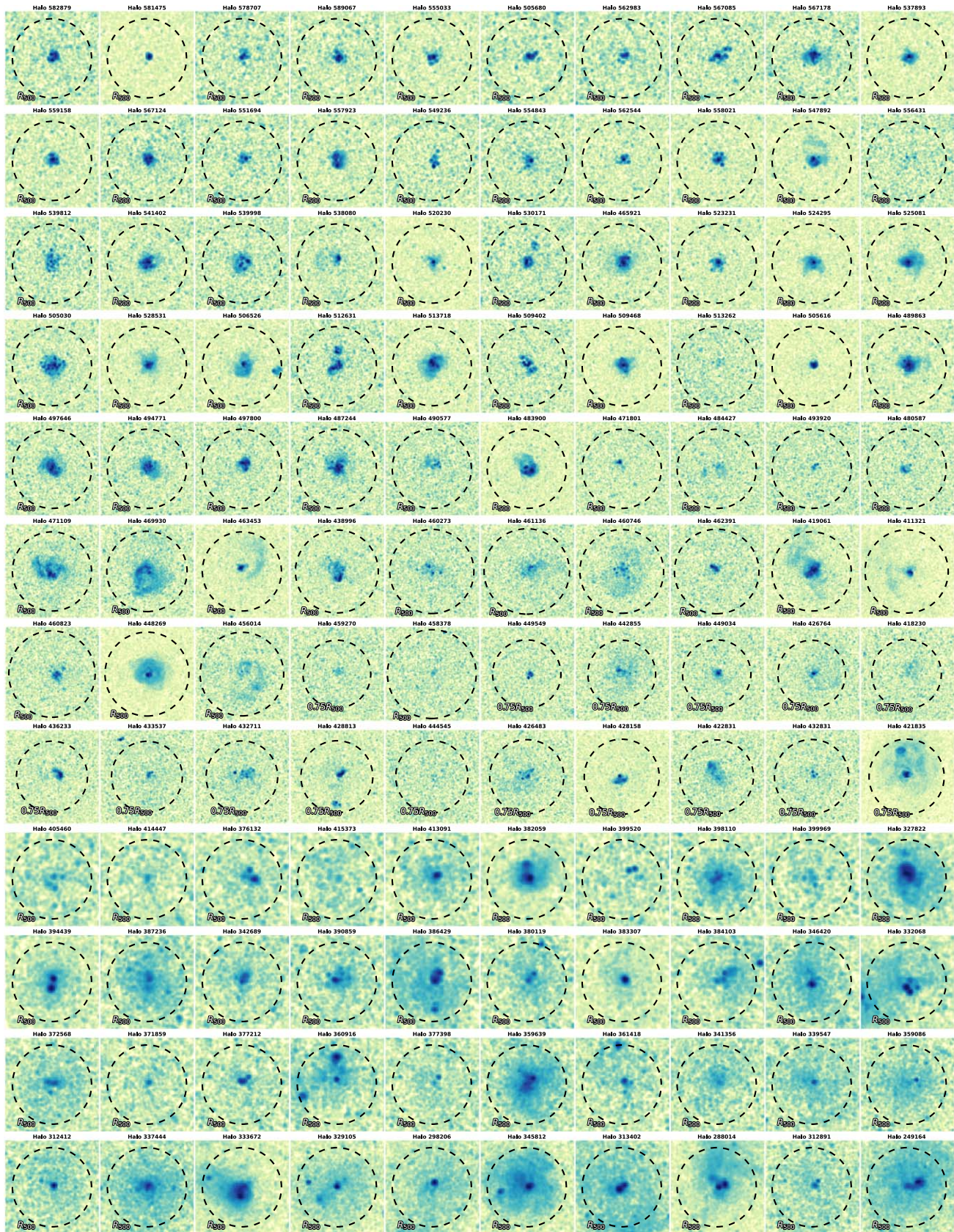
Figure 17. Stacked O VII(f) and O VIII images from mock observations of the TNG100 galaxy halos, shown in log-scale with a fraction of the characteristic radius R_{500} indicated.
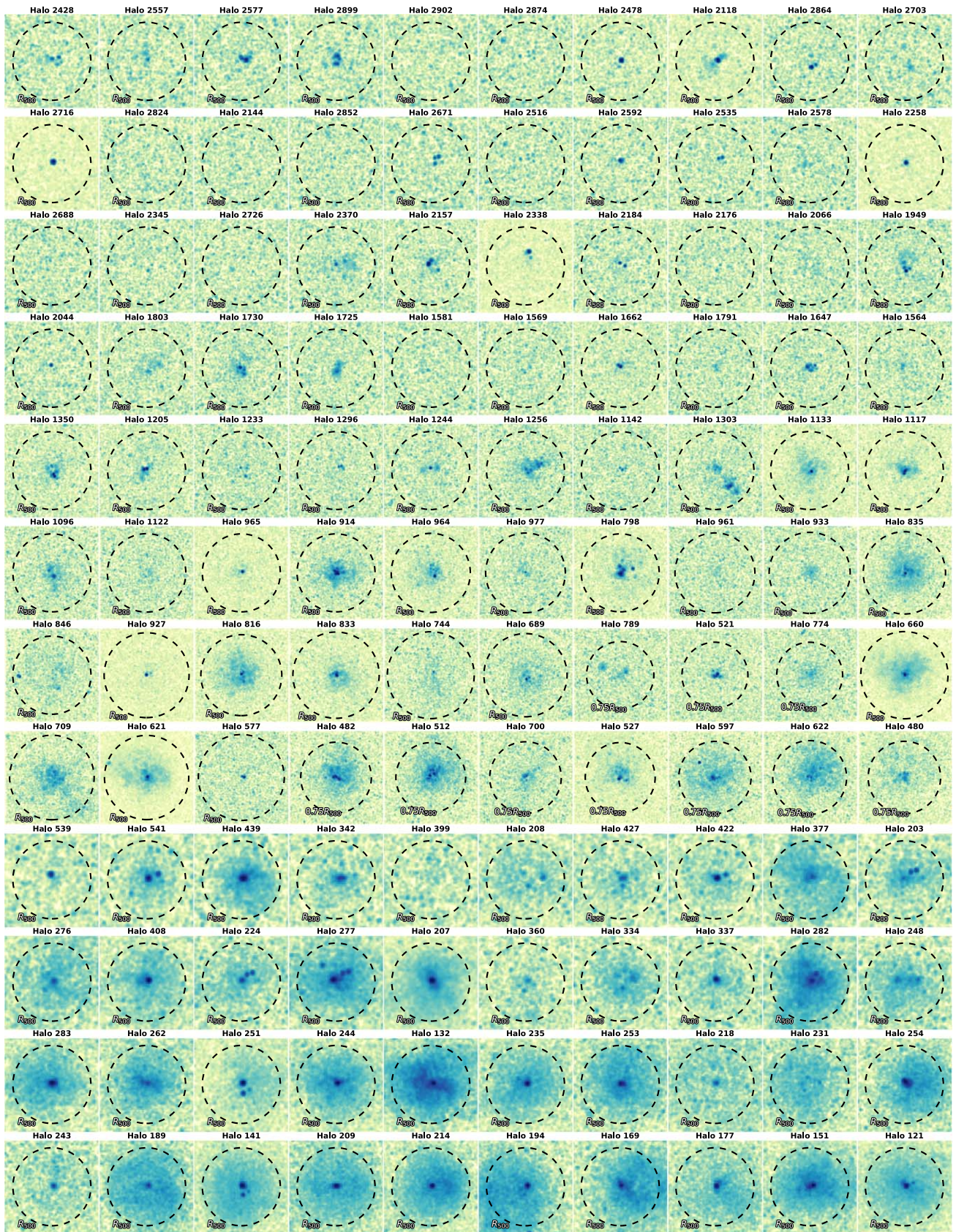
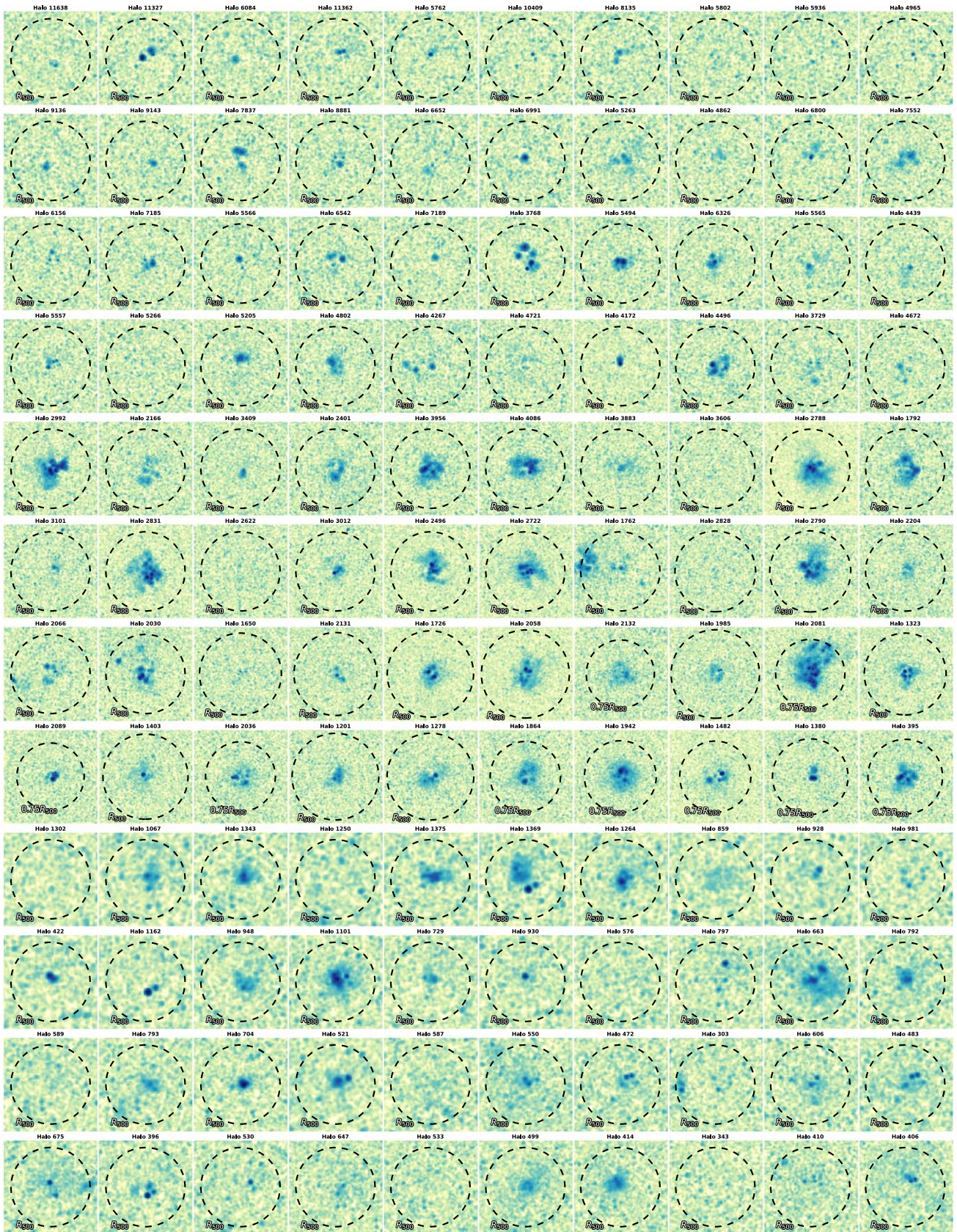**Figure 18.** The same as Figure 17, but for the EAGLE galaxy halos.

Figure 19. The same as Figure 17, but for the Simba galaxy halos.

ORCID iDs

Gerrit Schellenberger ⓘ https://orcid.org/0000-0002-4962-0740
Ákos Bogdán ⓘ https://orcid.org/0000-0003-0573-7733
John A. ZuHone ⓘ https://orcid.org/0000-0003-3175-2347
Benjamin D. Oppenheimer ⓘ https://orcid.org/0000-0002-3391-2116
Nhut Truong ⓘ https://orcid.org/0000-0003-4983-0462
Ildar Khabibullin ⓘ https://orcid.org/0000-0003-3701-5882
Fred Jennings ⓘ https://orcid.org/0009-0000-0152-9983
Annalisa Pillepich ⓘ https://orcid.org/0000-0003-1065-9274
Joseph Burchett ⓘ https://orcid.org/0000-0002-1979-2197
Christopher Carr ⓘ https://orcid.org/0000-0002-5840-0424
Priyanka Chakraborty ⓘ https://orcid.org/0000-0002-4469-2518
Robert Crain ⓘ https://orcid.org/0000-0001-6258-0344
William Forman ⓘ https://orcid.org/0000-0002-9478-1682
Christine Jones ⓘ https://orcid.org/0000-0003-2206-4243
Caroline A. Kilbourne ⓘ https://orcid.org/0000-0001-9464-4103
Ralph P. Kraft ⓘ https://orcid.org/0000-0002-0765-0511
Maxim Markevitch ⓘ https://orcid.org/0000-0003-0144-4052
Daisuke Nagai ⓘ https://orcid.org/0000-0002-6766-5942
Dylan Nelson ⓘ https://orcid.org/0000-0001-8421-5890
Anna Ogorzalek ⓘ https://orcid.org/0000-0003-4504-2557
Scott Randall ⓘ https://orcid.org/0000-0002-3984-4337
Arnab Sarkar ⓘ https://orcid.org/0000-0002-5222-1337
Joop Schaye ⓘ https://orcid.org/0000-0002-0668-5560
Sylvain Veilleux ⓘ https://orcid.org/0000-0002-3158-6820
Mark Vogelsberger ⓘ https://orcid.org/0000-0001-8593-7692
Q. Daniel Wang ⓘ https://orcid.org/0000-0002-9279-4041
Irina Zhuravleva ⓘ https://orcid.org/0000-0001-7630-8085

References

Al-Baidhany, I. A., Chiad, S. S., Jabbar, W. A., et al. 2020, in AIP Conf. Proc. 2290, Int. Conf. Numerical Analysis and Applied Mathematics ICNAAM 2019 (Melville, NY: AIP Publishing)
Anders, E., & Grevesse, N. 1989, GeCoA, 53, 197
Anderson, M. E., & Bregman, J. N. 2011, ApJ, 737, 22
Anderson, M. E., Bregman, J. N., & Dai, X. 2012, ApJ, 762, 106
Anderson, M. E., Churazov, E., & Bregman, J. N. 2015, MNRAS, 455, 227
Arnaud, K. A. 1996, in ASP Conf. Ser. 101, Astronomical Data Analysis Software and Systems V, ed. G. H. Jacoby & J. Barnes (San Francisco, CA: ASP), 17
Ayromlou, M., Nelson, D., & Pillepich, A. 2023, MNRAS, 524, 5391
Barret, D., Albouys, V., Herder, J.-W. D., et al. 2023, ExA, 55, 373
Barret, D., den Herder, J. W., Piro, L., et al. 2013, arXiv:1308.6784
Barret, D., Trong, T. L., den Herder, J.-W., et al. 2018, Proc. SPIE, 10699, 106991G
Behroozi, P., Wechsler, R. H., Hearin, A. P., & Conroy, C. 2019, MNRAS, 488, 3143
Behroozi, P. S., Conroy, C., & Wechsler, R. H. 2010, ApJ, 717, 379
Benson, A. J., Bower, R. G., Frenk, C. S., & White, S. D. M. 2000, MNRAS, 314, 557
Bhattacharyya, S., Das, S., Gupta, A., Mathur, S., & Krongold, Y. 2023, ApJ, 952, 41
Bluem, J., Kaaret, P., Kuntz, K. D., et al. 2022, ApJ, 936, 72
Bogdán, Á., Forman, W. R., Kraft, R. P., & Jones, C. 2013a, ApJ, 772, 98
Bogdán, Á., Forman, W. R., Vogelsberger, M., et al. 2013b, ApJ, 772, 97
Bogdán, Á., & Gilfanov, M. 2011, MNRAS, 418, 1901
Bogdan, A., Khabibullin, I., Kovacs, O., et al. 2023, arXiv:2306.05449
Bogdán, Á., Vogelsberger, M., Kraft, R. P., et al. 2015, ApJ, 804, 72
Booth, C. M., & Schaye, J. 2009, MNRAS, 398, 53
Bogdán, Á., Bourdin, H., Forman, W. R., et al. 2017, ApJ, 850, 98
Bregman, J. N., Hodges-Kluck, E., Qu, Z., et al. 2022, ApJ, 928, 14
Burke, D., Laurino, O., Wmclaugh, et al., 2020 sherpa/sherpa: Sherpa 4.12.1, v4.12.1, Zenodo, doi:10.5281/zenodo.3944985
Byrohl, C., & Nelson, D. 2023, MNRAS, 523, 5248
Canizares, C. R., Fabbiano, G., & Trinchieri, G. 1987, ApJ, 312, 503
Carlesi, E., Hoffman, Y., & Libeskind, N. I. 2022, MNRAS, 513, 2385

Carr, C., Bryan, G. L., Fielding, D. B., Pandya, V., & Somerville, R. S. 2023, ApJ, 949, 21
Cash, W. 1979, ApJ, 228, 939
Cen, R., & Ostriker, J. P. 1999, ApJ, 514, 1
Cen, R., & Ostriker, J. P. 2000, ApJ, 538, 83
Chadayammuri, U., Bogdán, Á., Oppenheimer, B. D., et al. 2022, ApJL, 936, L15
Chakraborty, P., Ferland, G. J., Chatzikos, M., Guzmán, F., & Su, Y. 2020a, ApJ, 901, 69
Chakraborty, P., Ferland, G. J., Chatzikos, M., Guzmán, F., & Su, Y. 2020b, ApJ, 901, 68
Chakraborty, P., Ferland, G. J., Chatzikos, M., et al. 2022, ApJ, 935, 70
Churazov, E., Haehnelt, M., Kotov, O., & Sunyaev, R. 2001, MNRAS, 323, 93
Comparat, J., Truong, N., Merloni, A., et al. 2022, A&A, 666, A156
Crain, R. A., McCarthy, I. G., Frenk, C. S., Theuns, T., & Schaye, J. 2010, MNRAS, 407, 1403
Crain, R. A., Schaye, J., Bower, R. G., et al. 2015, MNRAS, 450, 1937
Dai, X., Anderson, M. E., Bregman, J. N., & Miller, J. M. 2012, ApJ, 755, 107
Das, S., Chiang, Y.-K., & Mathur, S. 2023, ApJ, 951, 125
Das, S., Mathur, S., Gupta, A., Nicastro, F., & Krongold, Y. 2019a, ApJ, 887, 257
Das, S., Mathur, S., Gupta, A., & Krongold, Y. 2021, ApJ, 918, 83
Das, S., Mathur, S., Nicastro, F., & Krongold, Y. 2019b, ApJL, 882, L23
Davé, R., Anglés-Alcázar, D., Narayanan, D., et al. 2019, MNRAS, 486, 2827
Davies, J. J., Crain, R. A., McCarthy, I. G., et al. 2019a, MNRAS, 485, 3783
Davies, J. J., Crain, R. A., Oppenheimer, B. D., & Schaye, J. 2019b, MNRAS, 491, 4462
De Luca, A., & Molendi, S. 2004, A&A, 419, 837
Donnari, M., Pillepich, A., Nelson, D., et al. 2021, MNRAS, 506, 4760
Eckert, D., Molendi, S., Vazza, F., Ettori, S., & Paltani, S. 2013, A&A, 551, A22
Eckert, D., Roncarelli, M., Ettori, S., et al. 2015, MNRAS, 447, 2198
Ferland, Chatzikos, Guzmán, et al. 2017, RMxAA, 53, 385
Forman, W., Jones, C., & Tucker, W. 1985, ApJ, 293, 102
Foster, A., Smith, R., Brickhouse, N. S., et al. 2018, AAS Meeting, 231, 253.03
Foster, A. R., Ji, L., Smith, R. K., & Brickhouse, N. S. 2012, ApJ, 756, 128
Freeman, P., Doe, S., & Siemiginowska, A. 2001, Proc. SPIE, 4477, 76
Fruscione, A., McDowell, J. C., Allen, G. E., et al. 2006, Proc. SPIE, 6270, 62701V
Gavazzi, R., Treu, T., Rhodes, J. D., et al. 2007, ApJ, 667, 176
Geisler, D., Wallerstein, G., Smith, V. V., & Casetti-Dinescu, D. I. 2007, PASP, 119, 939
Goulding, A. D., Greene, J. E., Ma, C.-P., et al. 2016, ApJ, 826, 167
Guo, Q., White, S., Li, C., & Boylan-Kolchin, M. 2010, MNRAS, 404, 1111
Hansen, S. M., Sheldon, E. S., Wechsler, R. H., & Koester, B. P. 2009, ApJ, 699, 1333
Harris, C. R., Millman, K. J., van der Walt, S. J., et al. 2020, Natur, 585, 357
Harrison, C. M. 2017, NatAs, 1, 0165
Hickox, R. C., & Markevitch, M. 2006, ApJ, 645, 95
Hopkins, P. F. 2015, MNRAS, 450, 53
Hunter, J. D. 2007, CSE, 9, 90
Jansen, F., Lumb, D., Altieri, B., et al. 2001, A&A, 365, L1
Khabibullin, I., & Churazov, E. 2019, MNRAS, 482, 4972
Kim, D.-W., Anderson, C., Burke, D., et al. 2019, ApJS, 241, 36
Kim, D.-W., & Fabbiano, G. 2013, ApJ, 776, 116
Kraft, R., Markevitch, M., Kilbourne, C. & the LEM Team 2022, arXiv:2211.09827
Lehmer, B. D., Xue, Y. Q., Brandt, W. N., et al. 2012, ApJ, 752, 46
Li, J.-T. 2020, AN, 341, 177
Li, J.-T., Bregman, J. N., Wang, Q. D., Crain, R. A., & Anderson, M. E. 2018, ApJL, 855, L24
Li, J.-T., Bregman, J. N., Wang, Q. D., et al. 2017, ApJS, 233, 20
Li, Z., Wang, Q. D., & Hameed, S. 2007, MNRAS, 376, 960
Li, Z., Wang, Q. D., Irwin, J. A., & Chaves, T. 2006, MNRAS, 371, 147
Licquia, T. C., & Newman, J. A. 2015, ApJ, 806, 96
Lotti, S., D'Andrea, M., Molendi, S., et al. 2021, ApJ, 909, 111
Lumb, D. H., Schartel, N., & Jansen, F. A. 2012, arXiv:1202.1651
Macquart, J.-P., Prochaska, J. X., McQuinn, M., et al. 2020, Natur, 581, 391
Mandelbaum, R., Seljak, U., Kauffmann, G., Hirata, C. M., & Brinkmann, J. 2006, MNRAS, 368, 715
Marinacci, F., Vogelsberger, M., Pakmor, R., et al. 2018, MNRAS, 480, 5113
Mathews, W. G. 1990, ApJ, 354, 468
Mathews, W. G., & Brighenti, F. 2003, ARA&A, 41, 191
Mathur, S., Das, S., Gupta, A., & Krongold, Y. 2023, MNRAS Lett., 525, L11
Matthee, J., & Schaye, J. 2018, MNRAS Lett., 479, L34

McAlpine, S., Helly, J. C., Schaller, M., et al. 2016, A&C, 15, 72
McCammon, D., Almy, R., Apodaca, E., et al. 2002, ApJ, 576, 188
Meidinger, N., Barbera, M., Emberger, V., et al. 2017, Proc. SPIE, 10397, 103970V
Mernier, F., Cucchetti, E., Tornatore, L., et al. 2020, A&A, 642, A90
Mernier, F., de Plaa, J., Kaastra, J. S., et al. 2017, A&A, 603, A80
Mitchell, P. D., & Schaye, J. 2022, MNRAS, 511, 2948
Moser, E., Battaglia, N., Nagai, D., et al. 2022, ApJ, 933, 133
Moser, B. P., Somerville, R. S., Maulbetsch, C., et al. 2010, ApJ, 710, 903
Nagai, D., & Lau, E. T. 2011, ApJL, 731, L10
Naiman, J. P., Pillepich, A., Springel, V., et al. 2018, MNRAS, 477, 1206
Nelson, D., Byrohl, C., Ogorzalek, A., et al. 2023, MNRAS, 522, 3665
Nelson, D., Kauffmann, G., Pillepich, A., et al. 2018a, MNRAS, 477, 450
Nelson, D., Pillepich, A., Springel, V., et al. 2018b, MNRAS, 475, 624
Nelson, D., Pillepich, A., Springel, V., et al. 2019a, MNRAS, 490, 3234
Nelson, D., Springel, V., Pillepich, A., et al. 2019b, ComAC, 6, 2
Nica, A., Oppenheimer, B. D., Crain, R. A., et al. 2022, MNRAS, 517, 1958
Nicastro, F., Krongold, Y., Fang, T., et al. 2023, ApJL, 955, L21
Nomoto, K., Tominaga, N., Umeda, H., Kobayashi, C., & Maeda, K. 2006, NuPhA, 777, 424
Nulsen, P. E. J., Stewart, G. C., & Fabian, A. C. 1984, MNRAS, 208, 185
Oppenheimer, B. D., Bogdán, Á., Crain, R. A., et al. 2020, ApJL, 893, L24
Oppenheimer, B. D., Davies, J. J., Crain, R. A., et al. 2019, MNRAS, 491, 2939
O'Sullivan, E., David, L. P., & Vrtilek, J. M. 2013, MNRAS, 437, 730
O'Sullivan, E., Forbes, D. A., & Ponman, T. J. 2001, MNRAS, 328, 461
Péroux, C., Nelson, D., van de Voort, F., et al. 2020, MNRAS, 499, 2462
Pillepich, A., Nelson, D., Hernquist, L., et al. 2017a, MNRAS, 475, 648
Pillepich, A., Nelson, D., Springel, V., et al. 2019, MNRAS, 490, 3196
Pillepich, A., Springel, V., Nelson, D., et al. 2017b, MNRAS, 473, 4077
Pillepich, A., Springel, V., Nelson, D., et al. 2018, MNRAS, 473, 4077
Piro, L., den Herder, J. W., & Ohashi, T. 2007, NCimB, 122, 1011
Planelles, S., Borgani, S., Fabjan, D., et al. 2014, MNRAS, 438, 195
Planelles, S., Fabjan, D., Borgani, S., et al. 2017, MNRAS, 467, 3827
Ponti, G., Zheng, X., Locatelli, N., et al. 2023, A&A, 674, A195
Posti, L., & Helmi, A. 2019, A&A, 621, A56
Predehl, P., Andritschke, R., Arefiev, V., et al. 2021, A&A, 647, A1
Prochaska, J. X., Werk, J. K., Worseck, G., et al. 2017, ApJ, 837, 169
Putman, M. E., Peek, J. E. G., & Joung, M. R. 2012, ARA&A, 50, 491
Rahmani, S., Lianou, S., & Barmby, P. 2016, MNRAS, 456, 4128
Ramesh, R., Nelson, D., & Pillepich, A. 2022, MNRAS, 518, 5754
Rasia, E., Lau, E. T., Borgani, S., et al. 2014, ApJ, 791, 96
Ravi, V. 2019, ApJ, 872, 88
Revnivtsev, M., Sazonov, S., Churazov, E., et al. 2009, Natur, 458, 1142
Robson, D., & Davé, R. 2020, MNRAS, 498, 3061
Sato, K., Yamasaki, N. Y., Ishida, M., et al. 2022, JLTP, 209, 971
Schaller, M., Dalla Vecchia, C., Schaye, J., et al. 2015, MNRAS, 454, 2277
Schaye, J., Crain, R. A., Bower, R. G., et al. 2015, MNRAS, 446, 521
Schödel, R., Ott, T., Genzel, R., et al. 2002, Natur, 419, 694
Segers, M. C., Crain, R. A., Schaye, J., et al. 2016, MNRAS, 456, 1235
Simionescu, A., Allen, S. W., Mantz, A., et al. 2011, Sci, 331, 1576

Smith, R. K., Bautz, M., Bregman, J., et al. 2022, Proc. SPIE, 12181, 1218121
Sorini, D., Davé, R., Cui, W., & Appleby, S. 2022, MNRAS, 516, 883
Springel, V., Pakmor, R., Pillepich, A., et al. 2018, MNRAS, 475, 676
Tamm, A., Tempel, E., Tenjes, P., Tihhonova, O., & Tuvikene, T. 2012, A&A, 546, A4
Tashiro, M., Maejima, H., Toda, K., et al. 2018, Proc. SPIE, 10699, 520
Terada, Y., Holland, M., Loewenstein, M., et al. 2021, JATIS, 7, 037001
Terrazas, B. A., Bell, E. F., Pillepich, A., et al. 2020, MNRAS, 493, 1888
The Astropy Collaboration, Price-Whelan, A. M., Sipőcz, B. M., et al. 2018, AJ, 156, 123
The Astropy Collaboration, Robitaille, T. P., Tollerud, E. J., et al. 2013, A&A, 558, A33
Trinchieri, G., & Fabbiano, G. 1985, ApJ, 296, 447
Trinchieri, G., Fabbiano, G., & Canizares, C. R. 1986, ApJ, 310, 637
Truong, N., Pillepich, A., Nelson, D., Werner, N., & Hernquist, L. 2021, MNRAS, 508, 1563
Truong, N., Pillepich, A., Nelson, D., et al. 2023, MNRAS, 525, 1976
Truong, N., Pillepich, A., Werner, N., et al. 2020, MNRAS, 494, 549
Tumlinson, J., Thom, C., Werk, J. K., et al. 2011, Sci, 334, 948
van de Voort, F., & Schaye, J. 2013, MNRAS, 430, 2688
Vogelsberger, M., Genel, S., Springel, V., et al. 2014a, MNRAS, 444, 1518
Vogelsberger, M., Genel, S., Springel, V., et al. 2014b, Natur, 509, 177
Vogelsberger, M., Marinacci, F., Torrey, P., & Puchwein, E. 2020, NatRP, 2, 42
Vogelsberger, M., Marinacci, F., Torrey, P., et al. 2018, MNRAS, 474, 2073
Wang, L., & Jing, Y. P. 2010, MNRAS, 402, 1796
Wang, Q. D., Immler, S., Walterbos, R., Lauroesch, J. T., & Breitschwerdt, D. 2001, ApJL, 555, L99
Weinberger, R., Springel, V., Hernquist, L., et al. 2017, MNRAS, 465, 3291
Werk, J. K., Xavier Prochaska, J., Cantalupo, S., et al. 2016, ApJ, 833, 54
Werk, J. K., Xavier Prochaska, J., Tumlinson, J., et al. 2014, ApJ, 792, 8
Werner, N., de Plaa, J., Kaastra, J. S., et al. 2006, A&A, 449, 475
White, S. D. M., & Frenk, C. S. 1991, ApJ, 379, 52
White, S. D. M., & Rees, M. J. 1978, MNRAS, 183, 341
Wijers, N. A., & Schaye, J. 2022, MNRAS, 514, 5214
Wilms, J., Allen, A., & McCray, R. 2000, ApJ, 542, 914
Wu, X., & McQuinn, M. 2023, ApJ, 945, 87
Wu, X., Mo, H., Li, C., & Lim, S. 2020, ApJ, 903, 26
Xavier Prochaska, J., Weiner, B., Chen, H.-W., Mulchaey, J., & Cooksey, K. 2011, ApJ, 740, 91
Zhang, Y., Comparat, J., Ponti, G., et al. 2024, arXiv:2401.17308
Zhang, Y.-N., Li, C., Xu, D., & Cui, W. 2022, ExA, 53, 1053
Zheng, Z., Coil, A. L., & Zehavi, I. 2007, ApJ, 667, 760
Zhuravleva, I., Churazov, E., Arévalo, P., et al. 2015, MNRAS, 450, 4184
Zinger, E., Pillepich, A., Nelson, D., et al. 2020, MNRAS, 499, 768
ZuHone, J. A., & Hallman, E. J., 2016 pyXSIM: Synthetic X-ray observations generator, Astrophysics Source Code Library, ascl:1608.002
ZuHone, J. A., Schellenberger, G., Ogorzalek, A., et al. 2023a, ApJ, 967, 49
ZuHone, J. A., Vikhlinin, A., Tremblay, G. R., et al., 2023b SOXS: Simulated Observations of X-ray Sources, Astrophysics Source Code Library, ascl:2301.024